

1 **Mapping snow depth within a tundra ecosystem using multiscale observations and**  
2 **Bayesian methods**

3

4 Haruko M. Wainwright

5 [hmwainwright@lbl.gov](mailto:hmwainwright@lbl.gov)

6 Earth Sciences Division, Lawrence Berkeley National Laboratory

7 1 Cyclotron Road, MS 74R-316C, Berkeley, CA 94720-8126

8

9 Anna K. Liljedahl

10 [akliljedahl@alaska.edu](mailto:akliljedahl@alaska.edu)

11 Water & Environmental Research Center

12 University of Alaska Fairbanks

13 306 Tanana Loop, Fairbanks, AK 99775-5860, USA

14

15 Baptiste Dafflon

16 [bdafflon@lbl.gov](mailto:bdafflon@lbl.gov)

17 Earth Sciences Division, Lawrence Berkeley National Laboratory

18 1 Cyclotron Road, MS 74R-316C, Berkeley, CA 94720-8126

19

20 Craig Ulrich

21 [CUlrich@lbl.gov](mailto:CUlrich@lbl.gov)

22 Earth Sciences Division, Lawrence Berkeley National Laboratory

23 1 Cyclotron Road, MS 74R-316C, Berkeley, CA 94720-8126

24

25 John E. Peterson

26 [jepeterson@lbl.gov](mailto:jepeterson@lbl.gov)

27 Earth Sciences Division, Lawrence Berkeley National Laboratory

28 1 Cyclotron Road, MS 74R-316C, Berkeley, CA 94720-8126

29

30 Susan S. Hubbard

31 [sshubbard@lbl.gov](mailto:sshubbard@lbl.gov)

32 Earth Sciences Division, Lawrence Berkeley National Laboratory

33 1 Cyclotron Road, MS 74R-316C, Berkeley, CA 94720-8126

34

35 **Abstract**

36 This paper compares and integrates different strategies to characterize the variability of end-of-  
37 winter snow depth and its relationship to topography in ice-wedge polygon tundra of Arctic  
38 Alaska. Snow depth was measured using *in situ* snow depth probes, and estimated using ground  
39 penetrating radar (GPR) surveys and the Photogrammetric Detection and Ranging (PhoDAR)  
40 technique with an unmanned aerial system (UAS). We found that GPR data provided high-  
41 precision estimates of snow depth (RMSE = 2.9 cm), with a spatial sampling of 10 cm along  
42 transects. PhoDAR-based approaches provided snow depth estimates in a less laborious manner  
43 compared to GPR and probing while yielding a high precision (RMSE = 6.0 cm) and a fine  
44 spatial sampling (4 cm by 4 cm). We then investigated the spatial variability of snow depth and  
45 its correlation to micro- and macrotopography using the snow-free LiDAR digital elevation map  
46 (DEM) and the wavelet approach. We found that the end-of-winter snow depth was highly  
47 variable over short (several meter) distances, and the variability was correlated with  
48 microtopography. Microtopographic lows (i.e., troughs and centers of low-centered polygons)  
49 were filled in with snow, which resulted in a smooth and even snow surface following  
50 macrotopography. We developed and implemented a Bayesian approach to integrate the snow-  
51 free LiDAR DEM and multi-scale measurements (probe and GPR) as well as the topographic  
52 correlation for estimating snow depth over the landscape. Our approach led to high precision  
53 estimates of snow depth (RMSE = 6.0 cm), at 0.5-meter resolution and over the LiDAR domain  
54 (750 m by 700 m).

55

56 **1. Introduction**

57 Snow plays a critical role in ecosystem functioning of the Arctic tundra environment through its  
58 impacts on soil hydrothermal processes and energy exchange (e.g., Callaghan et al., 2011). Snow  
59 insulates the ground from intense cold during the Arctic winter, limiting the heat transfer  
60 between the air and the ground (Zhang, 2005). Snow depth affects active layer and permafrost  
61 temperatures throughout the year (Gamon et al., 2012; Stieglitz et al., 2003), and increased snow  
62 depth has resulted in permafrost degradation (Osterkamp, 2007). Snow's insulating capacity  
63 enhances conditions for active soil microbial processes and CO<sub>2</sub>/CH<sub>4</sub> production during winter  
64 (Nobrega and Grogan, 2007; Schimel et al., 2004; Clein and Schimel, 1995; Jansson and Taş,  
65 2014; Zona et al., 2016). In addition, snow serves as an important water source to tundra  
66 ecosystems during the growing season, and therefore has a large impact on biological processes  
67 via hydrology. Snowmelt water can lead to extensive inundation of low-gradient tundra and large  
68 runoff events in early summer (Bowling et al., 2003; Kane et al., 1991; Liljedahl et al., 2016).  
69 Since soil biogeochemistry and vegetation are controlled by soil moisture (Sjögersten et al.,  
70 2006; Wainwright et al., 2015), the amount of snow affects ecosystem functioning throughout  
71 the season.

72

73 In order to investigate controls of snow on ecosystem properties, high resolution estimates of  
74 snow are needed over large spatial regions. This is especially true in ice-wedge polygon tundra,  
75 which dominates a large portion of the high Arctic (Zona et al., 2011). The ice wedges develop  
76 when frost cracks occur in the ground, and vertical ice wedges grow laterally over years  
77 (Leffingwell, 1915; MacKay, 2000). Soil movement associated with ice-wedge development  
78 creates small-scale topographic variations – *microtopography* – where the ground surface

79 elevation can vary significantly over lateral length distances of several meters (e.g., Brown,  
80 1967; MacKay, 2000; Engstrom et al., 2005; Zona et al., 2011). This microtopography leads to  
81 dramatically variable snow depth across short distances. Liljedahl et al. (2016) found that the  
82 differential snow distribution increased the partitioning of snowmelt water into runoff, leading to  
83 less water stored on the tundra landscape. Gamon et al. (2012) reported that snow depth  
84 heterogeneity results in differential thawing and active layer thickness variability. In addition,  
85 there is large-scale topographic variability at the scale of several hundred meters to kilometers –  
86 *macrotopography* –which is often associated with drained thaw lake basins or drainage features  
87 (Hinkel et al., 2003). Although the effect of macrotopography on snow depth has not been  
88 studied, Engstrom et al. (2005) quantified that both macrotopography and microtopography have  
89 a significant effect on soil moisture distribution. The snow representation of the Arctic tundra  
90 needs to be refined to account for the effect of such multiscale terrain heterogeneities on  
91 hydrology and ecosystem functioning, by bridging between finer geographical scales (several  
92 meters) and large areal coverage (several hundred meters to kilometers).

93  
94 Snow depth characterization in Arctic tundra environments has traditionally been performed  
95 using snow depth probes (Benson and Sturm, 1993; Hirashima et al., 2004; Derksen et al., 2009;  
96 Rees et al., 2014; Dvornikov et al., 2015), or modeled using terrain and vegetation information  
97 (Sturm and Wagner, 2010; Liston et al., 1998; Pomeroy et al., 1997). Recently, there have been  
98 several new techniques for estimating snow depth in high resolution, and in a non-invasive and  
99 spatially extensive manner. Ground-penetrating radar (GPR) has been widely used to  
100 characterize snow cover in alpine, arctic and glacier environments (e.g., Harper and Bradford,  
101 2003; Machguth et al., 2006; Gusmeroli and Grosse, 2012; Gusmeroli et al., 2014). GPR

102 measures the radar reflection from the snow-ground interface, which can be used to estimate  
103 snow depth. GPR can be collected by foot, snowmobile or airborne methods. In addition, Light  
104 Detection and Ranging (LiDAR) and Photogrammetric Detection and Ranging (PhoDAR)  
105 airborne methods have recently been used to estimate snow depth at local and regional scales  
106 (e.g., Deems et al., 2013; Harpold et al., 2014; Nolan et al., 2015). Both techniques measure the  
107 snow surface elevation, using laser in LiDAR, or a camera with a structure-from-motion (SfM)  
108 algorithm in PhoDAR. Both approaches allow us to estimate snow depth by subtracting the  
109 snow-free elevation from the snow surface elevation. While there is potential for providing  
110 detailed information about local-scale snow variability using LiDAR and PhoDAR snow depth  
111 estimates, these techniques have not been extensively tested in ice-wedge-polygonal tundra  
112 environments.

113  
114 Such indirect geophysical methods are, however, known to have increased snow depth  
115 uncertainty relative to direct measurements (here ground-based snow depth probe measurements)  
116 (e.g., Hubbard and Rubin, 2005). The uncertainty of the snow depth probe measurements is sub-  
117 centimeter to several centimeters depending on the surface vegetation (Berezovskaya and Kane,  
118 2007). On the other hand, the snow depth estimates obtained using GPR can be affected by  
119 uncertainty associated with radar velocity, which depends on snow density (Harper and  
120 Bradford, 2003). In the environments with complex terrain such as ice-wedge polygonal tundra,  
121 GPR-based snow estimates could also be influenced by the errors stemming from radar  
122 positioning and raypath assumptions. The airborne LiDAR/PhoDAR-based methods are subject  
123 to the errors associated with georeferencing, processing and calibration (e.g., Deems et al., 2013;

124 Nolan et al., 2015). The accuracy of the airborne methods is usually several tens of centimeters,  
125 which is lower than the snow depth probe measurements.

126

127 Integrating different types of snow measurements can take advantage of the strengths of various  
128 techniques while minimizing the limitations stemming from using a single method. Bayesian  
129 approaches have proven to be useful for integrating multiscale, multi-type datasets to estimate  
130 spatially heterogeneous terrestrial system parameters in a manner that honors method-specific  
131 uncertainty (e.g., Wikle et al., 2001; Wainwright et al., 2014; 2016). Bayesian methods also  
132 permit systematic incorporation of expert knowledge or process-specific information, such as the  
133 relationships between datasets and parameters. In particular, snow depth is known to be affected  
134 by topography and wind direction (e.g., Benson and Sturm, 1993; Anderson et al., 2014;  
135 Dvornikov et al., 2015). To our knowledge, such Bayesian data integration methods have never  
136 been applied to estimate end-of-winter snow variability using multiple types of datasets.

137

138 The primary objectives of this study are to (1) compare point-scale snow depth probe, GPR and  
139 UAS-based PhoDAR approaches for characterizing snow depth, and the associated resolution  
140 and accuracy of the GPR and PhoDAR methods; (2) quantify the spatial variability of end-of-  
141 winter snow depth in ice-wedge polygonal tundra landscape; (3) explore the relationship between  
142 snow depth and topography; and (4) develop a Bayesian method to integrate multiscale, multi-  
143 type data to estimate snow depth over a LiDAR DEM covering an ice-wedge polygonal tundra  
144 landscape. In Section 2, we describe our site and datasets, including snow depth probes, ground-  
145 based GPR and UAS-based PhoDAR. In Section 3, we present the methodology to analyze the  
146 indirect snow depth measurements from GPR and PhoDAR as well as to evaluate the

147 heterogeneity of snow depth in relation to both microtopography (i.e., ice-wedge polygons) and  
148 macrotopography (i.e., large-scale gradient, drained thaw lake basins and interstitial upland  
149 tundra). We then develop a Bayesian geostatistical approach to integrate the multiscale datasets  
150 to estimate snow depth over the LiDAR domain. The snow measurement and estimation results  
151 are presented in Section 4 and discussed in Section 5.

152 **2. Data and Site Descriptions**

153 **2.1. Study Site**

154 Snow survey data were collected within a study site (approximately 750 m by 700 m) located on  
155 the Barrow Environmental Observatory near Barrow, Alaska, as part of the Department of  
156 Energy's Next-Generation Ecosystem Experiment (NGEE) Arctic project (Figure 1). This study  
157 domain has been characterized intensively in the NGEE-Arctic project, leading to various  
158 ecosystem and subsurface datasets, including snow depth measurements (Wainwright et al.,  
159 2015; Dafflon et al., 2016). Mean annual air temperature at the Barrow site is  $-11.3^{\circ}\text{C}$  and mean  
160 annual precipitation is 173 mm (Liljedahl et al., 2011). Snowmelt usually ends in early to mid-  
161 June. The wind direction is predominantly from east to west throughout the year.

162

163 Ice-wedge polygons are prevalent in the region, including low-centered polygons in drained thaw  
164 lake basins and high-centered polygons with well-developed troughs in the upland tundra  
165 (Hinkel et al., 2003; Wainwright et al., 2015). The dominant plants are mosses (*Dicranum*  
166 *elongatum*, *Sphagnum*), lichens and vascular plants (such as *Carex aquatilis*); plant distribution  
167 at the site is governed by surface moisture variability (e.g., Hinkel et al., 2003; Zona et al.,  
168 2011). There are currently no tall shrubs or woody plants established within the study site,  
169 therefore complex topography is most likely to control the snow depth distribution within the  
170 study domain (Sturm et al., 2005; Dvornikov et al., 2015).

171

172 Three long transects and four representative plots were chosen within the study site to explore  
173 snow variability and its relationship to topography (Figure 1). Typical for low-gradient tundra  
174 terrain, ice-wedge polygon microtopographic variations are superimposed on macrotopographic

175 trends at the study site. The elevation is higher in the center of the domain (interstitial upland  
176 tundra) and lower near the drainage features in the south. The elevation is also relatively lower in  
177 the drained thaw lake basins (DTLB) region, which is located in the northeastern and  
178 northwestern edges of the study site. The four intensive plots (A-D), each 160m x 160m, were  
179 chosen to represent specific polygon types or macrotopographic positions within the study area.  
180 The three parallel transects, each ~500m long, were designed to traverse multiple polygon types  
181 in a continuous fashion (Hubbard et al., 2013). We refer to those transects by “the 500-meter  
182 transects”.

183

## 184 **2.2. Datasets**

185 Airborne LiDAR data were collected at the site on October 4th, 2005, and used to provide a  
186 high-resolution digital elevation map (DEM) of the snow-free ground at 0.5 m by 0.5 m  
187 resolution (Hubbard et al., 2013). The DEM effectively resolves both micro- and  
188 macrotopography at the study site (Figure 1). The original reported accuracy is 0.3 m in the  
189 horizontal direction and 0.15 m in the vertical direction. To further evaluate the accuracy of the  
190 airborne DEM, we measured the ground surface elevation in September 2011 at 1286 points  
191 around the 500-meter transects, using a high-precision centimeter-grade RTK Differential GPS  
192 (DGPS) system (the reported precision about 2 cm in the horizontal direction and 3 cm in the  
193 vertical direction). The root mean square error of the LiDAR DEM compared to the DGPS data  
194 was 6.08 cm.

195

196 The majority of the snow depth data was collected on May 6–12, 2012, during which no snowfall  
197 occurred and little change in snow depth was observed. Snow depth was measured in the four

198 intensive study plots and along three transect lines (Figure 1). Two sets of snow depth  
199 measurements using a snow depth probe were collected. The ‘fine-grid’ dataset was aimed to  
200 characterize the fine-scale heterogeneity by ~7200 snow depth point measurements (every  
201 ~0.3 m along transects with a 4 m spacing) across a small domain (~50 × 50 m) within Plots A-  
202 D. This was done using a GPS snow depth probe (Magnaprobe by Snow-Hydro) which had a  
203 reported vertical precision of < 0.01 m and horizontal precision of 2–10 m. The corner  
204 coordinates within each grid were surveyed with the RTK DGPS, while each snow depth point  
205 measurement was associated with latitude/longitude positional information recorded by the  
206 Magnaprobe’s built-in GPS receiver. All the snow depth point measurements were made along  
207 regularly spaced transects. Comparisons between coordinates surveyed with both the RTK DGPS  
208 and the Magnaprobe’s built-in GPS confirmed constant biases in the horizontal directions, which  
209 allowed a constant bias adjustment for all GPS surveyed snow depth point measurements.

210

211 A second ‘coarse-grid’ set of snow depth measurements covered the entire area in Plots A-D  
212 (~160 m × 160 m) with lower sampling density. The coarse-grid snow data were collected using  
213 a tile probe, which had a precision of approximately 0.01 m. Snow depth was measured every  
214 8 m along a measurement tape along five parallel transects in the coarse grid, which were spaced  
215 40 m apart. The total number of data points was 380 (95 points in each plot). Along the 500-  
216 meter transects, we used the tile probe along with a measurement tape, and measured eight points  
217 along each of the three lines. The start and end coordinates of each transect were surveyed with a  
218 RTK DGPS and used to georeference the measurement locations.

219

220 Ground-based ground penetrating radar (GPR) data were acquired over the four study plots and  
221 along the three 500-meter transects. The instrument (Mala ProEx with 500 MHz antenna) was  
222 pulled on a sled. In each plot, we acquired the GPR data at 0.1-m intervals (triggered by an  
223 odometer wheel) along 37 lines of 4-m spacing. The start and end coordinates of each transect  
224 were surveyed with a RTK DGPS and used to georeference the measurement locations. We  
225 compared the distance from wheel with the distance on tape and confirmed that the difference is  
226 generally very small at this site. The error of horizontal positioning is estimated to be about 0.1  
227 m. Several of the GPR lines were co-located with the ‘coarse-grid’ snow depth probe  
228 measurements. The GPR technique allowed for denser sampling within the plot relative to the  
229 snow depth probe, with more than 50,000 points in each plot. Due to the microtopography at this  
230 site, the positioning errors between in situ measurements and GPR data could lead to an error in  
231 the radar velocity and snow depth estimation. We evaluate the effect of such positioning errors  
232 extensively, as described in Section 3.1.

233

234 The GPR reflection signal from the bottom of snowpack (i.e., the ground surface) was clear,  
235 which allowed us to measure the travel time between the top and bottom of snowpack. The GPR  
236 processing routine consisted of (1) zero-time adjustment, (2) average tracer removal, (3) picking  
237 the travel time (manually with automated snapping in the ProMAX® software) of the reflected  
238 GPR signal that travelled from the snow surface to the snow-ground interface and back to the  
239 snow surface and (4) dividing by two to obtain a one-way travel time between the snow surface  
240 and ground surface. We processed the GPR data including travel-time picking before accounting  
241 for topography. More details on GPR processing and theory can be found in Annan (2015) and  
242 Jol (2009), while more detailed explanation on the use of GPR in the tundra can be found in

243 Hubbard et al. (2013). Differing from previous studies (e.g., Harper and Bradford, 2003), we did  
244 not observe echoes from snow layering. This is possibly because of the low antenna frequency  
245 (500 MHz), relatively thin snow layers (if present), and the low contrast between various snow  
246 layers. In addition, hoar layers or ice layers were not visible in our data or sensed using the  
247 probe. Although ice may form at the ground surface, causing the uncertainty of a few  
248 centimeters, we did not consider this effect in this study.

249  
250 Additional campaigns were carried out in 2013 – 2015 along the 500-meter transects only. UAS-  
251 based PhoDAR data were collected in July 2013 and 2014 to estimate snow-free ground surface  
252 elevation and in May 2015 for estimating snow depth along the transects. To make these  
253 measurements, we lifted a consumer-grade digital camera (Sony Nex-5R) to about 40 meters  
254 above the ground surface using a kite, and acquired downward-looking Red-Green-Blue  
255 landscape images, as well as collected some surface elevation data (method described in Smith et  
256 al., 2009). The reconstruction procedure was performed using a commercial computer vision  
257 software package (PhotoScan from Agisoft LLC). Reconstruction involved automatic image  
258 feature detection/matching, structure-from-motion and multiview-stereo techniques for 3D point-  
259 cloud generation, and georeferenced mosaic reconstruction (Nolan et al., 2015). High-accuracy  
260 georeferencing was enabled by using a network of ground control points placed on the ground  
261 (in summer) and on the snow (in winter) that were surveyed with a high-precision centimeter-  
262 grade RTK DGPS system. The reconstructed PhoDAR surface elevation models at this site show  
263 a resolution of 4 cm by 4 cm. We investigated the accuracy in detail as described in Section 3.2.

264

265 The snow-free ground surface elevation measurements were then subtracted from the snow  
266 surface data to estimate the snow depth over the area. The snow depth probe measurements were  
267 taken at 183 locations along one of the 500-meter transects to validate the PhoDAR-based snow  
268 depth estimates. The locations were marked on a measurement tape, the start and end coordinates  
269 of which were surveyed with a RTK DGPS and used to georeference the measurement locations.

## 270 **3. Methodology**

### 271 **3.1. GPR Snow Depth Analysis**

272 Snow depth can be inferred by multiplying GPR one-way travel time by radar velocity. The radar  
273 velocity is determined by the dielectric constant, which depends on snow density in dry snow  
274 (Tiuri, et al., 1984; Harper and Bradford, 2003). Depending on site conditions, the snow density  
275 can vary in both vertical and horizontal directions (Proksch et al., 2015). In this study, we  
276 assume that the depth-averaged radar velocity—which is a function of depth-averaged snow  
277 density—is sufficient for estimating snow depth. Thus, we compute the radar velocity based on  
278 the known snow depth from co-located snow depth probe measurements as: (radar velocity) =  
279 (probe-based snow depth)/(GPR one-way travel time). In addition, we investigate whether the  
280 lateral variations in snow density are significant at our site.

281  
282 Identifying co-located points between the GPR and snow depth probe measurements, however, is  
283 not a trivial task in polygonal ground, since the topography and snow depth can vary  
284 significantly within a meter. To address these issues, we investigate the correlations between the  
285 radar velocity and the submeter-scale variability of topography. To link the DEM elevation data  
286 to the snow depth probe and GPR data, we selected the DEM elevation (0.5 m by 0.5 m  
287 resolution) and GPR measurement at the nearest locations to the tile probe measurements. We  
288 assume that the effect of positioning errors is larger near the edge of polygons, or in the region  
289 where the submeter-scale topographic variability is high. We consider that the uncertainty of  
290 radar velocity can be reduced by not using the co-located snow depth probe measurements in  
291 regions of high submeter-scale variability. To define the submeter-scale variability, we compute  
292 the elevation difference within a 1-meter radius of each snow depth probe measurement. In

293 addition, the reflections from the troughs could originate from the edge of polygons rather than  
294 the location right below the GPR instrument. Such an “edge reflection” effect can lead to  
295 overestimation of the radar velocity. We assume that we could detect the presence of the edge  
296 reflection by evaluating the systematic bias (i.e., underestimation) in the radar velocity in relation  
297 to the submeter-scale topographic variability.

298

### 299 **3.2. UAS-based PhoDAR Snow Depth Analysis**

300 We first evaluate the accuracy of the PhoDAR-derived digital surface model (DSM) by  
301 comparing it to the RTK GPS elevation measurements along the 500-meter transects acquired in  
302 2011. Since the PhoDAR-derived DSM was obtained at very high lateral resolution (4 cm by 4  
303 cm), it was more prone to noise or small-scale variability (Nolan et al., 2015). As such, we test  
304 three schemes to explore the vertical agreement between the two datasets: (1) nearest points, (2)  
305 average elevation within the 0.5-m radius, and (3) minimum elevation within the 0.5-m radius.  
306 We use the same scheme (the best scheme among the three) for determining the snow-free and  
307 snow surface elevation at the co-located points. We then compare the snow depth estimates from  
308 PhoDAR and snow depth probe measurements at co-located points (the May-2015 snow data).  
309 Since we assume that the PhoDAR snow depth estimates would suffer from the same positioning  
310 errors associated with the snow depth probe data as GPR, we eliminate the snow depth probe  
311 measurements in the regions where the submeter-scale topographic variability is high.

312

### 313 **3.3. Spatial Variability Analysis of Topography and Snow Depth**

314 To quantify the topographic effects in a complex terrain of ice-wedge polygons and to partition  
315 micro- and macrotopography, we apply the wavelet transform method to the airborne LiDAR

316 DEM, which is commonly used for 2D image processing. The wavelet approach has been  
317 applied to DEM for geomorphic studies, including terrain analysis and landslide analysis (Bjørke  
318 and Nilsen, 2003; Kalbermatten, 2010; Kalbermatten et al., 2012). In this transform, a high-pass  
319 filter (a mother wavelet) and a low-pass filter (a father wavelet) are applied to decompose the  
320 DEM into four images at each scale: low-pass, high-pass horizontal, high-pass vertical, and high-  
321 pass diagonal images). The scale is a parameter in the wavelet transform, representing the width  
322 of the filter and the scale of topographic variability (Kalbermatten et al., 2012). Depending on  
323 the scale of the wavelet transform, the method yields different images, corresponding to different  
324 scales of topographic features. We define this wavelet scale as a *topography separation scale*.  
325 We consider the low-pass image as *macrotopographic elevation* (i.e., the smoothed version of  
326 the original DEM) and the high-pass diagonal image as *microtopographic elevation* (i.e., the  
327 topographic variability associated with ice-wedge polygon development). Removing the large-  
328 scale topography has been done in the previous studies in order to capture or quantify the effect  
329 of microtopography on carbon fluxes (Wainwright et al., 2015) or soil properties (Gillin et al.,  
330 2015).

331

332 Correlations between the topographic metrics and snow depth are identified using the Pearson  
333 product-moment correlation coefficient (Anderson et al., 2014). At each spatial scale, we can  
334 compute micro- and macrotopographic metrics such as slope and curvature as well as their  
335 correlations with corresponding probe-measured snow depth. The curvature is of particular  
336 interest, since Dvornikov et al. (2015) reported strong correlations between snow surface  
337 curvature and snow depth, and a dependency of this correlation on the DEM resolution (the  
338 lower resolution led to lower correlation coefficients). Note that the DEM resolution (0.5 m) in

339 this study is much finer than the one (25 m) in Dvornikov et al. (2015). We compute a wind  
340 factor in a similar manner as Dvornikov et al. (2015), with a slight modification. Here we define  
341 the wind factor as the inner product of the slope direction and predominant wind direction. With  
342 this calculation, the wind factor is smallest in the slope against the wind direction, and largest in  
343 the slope in line with the wind, which is reasonable and also consistent with visual observations  
344 at the site. When the correlation is statistically significant, the metrics are included in a  
345 regression analysis (Davison, 2003) to represent the snow depth as a function of the topographic  
346 metrics.

347

348 A geostatistical approach has been used to investigate the spatial variability of snow depth as  
349 well as the scales of variability (Anderson et al., 2014). The standard geostatistical analysis starts  
350 with creating an empirical variogram, followed by estimating the spatial correlation parameters  
351 (Diggle and Ribeiro, 2007). The spatial correlation parameters include (1) magnitude of  
352 variability (or spatial heterogeneity) as variance, (2) fraction of correlated and uncorrelated  
353 variability (nugget ratio), (3) spatial correlation length (range), and (4) covariance model (i.e.,  
354 the shape of decay in the spatial correlation as a function of distance), such as exponential and  
355 spherical models. The covariance models (equivalent to variogram models) can be selected to  
356 minimize the weighted sum of squares during variogram fitting.

357

358 Such spatial variability and correlation are particularly important for interpolating the sparse in  
359 situ snow depth measurements. The interpolation can be applied not only for snow depth itself  
360 but also for snow surface (snow depth plus elevation) or residual snow depth after removing  
361 topographic correlations in the regression analysis. The same geostatistical analysis method is

362 therefore performed for snow surface and residual snow depth. We used the geoR package in  
363 statistical software R (Ribeiro and Diggle, 2001; <https://www.r-project.org/>).

364

### 365 **3.4. Bayesian Geostatistical Estimation Method**

366 We first define that the snow depth at each pixel  $y_i$  ( $i = 1, \dots, n$ ) is a hidden variable which can be  
367 observed only with an added measurement error. In this study, we set the pixel size to 0.5 by  
368 0.5 m, which corresponded to the LiDAR DEM resolution. The snow depth distribution (or field)  
369 is defined by a vector  $\mathbf{y} = \{y_i | i = 1, \dots, n\}$ . We integrate three datasets: snow depth probe data  $\mathbf{z}_p$ ,  
370 GPR data  $\mathbf{z}_g$ , and LiDAR DEM  $\mathbf{z}_d$ . The goal of the estimation is to determine the posterior  
371 distribution of snow depth conditioned on all the given datasets,  $p(\mathbf{y} | \mathbf{z}_p, \mathbf{z}_g, \mathbf{z}_d)$ . Following a  
372 Bayesian hierarchical approach, we divide this posterior distribution into three sets of statistical  
373 sub-models (Wikle et al., 2001; Wainwright et al., 2014; 2016). First, *data models* represent each  
374 data value as a function of snow depth at each pixel, depending on different data types. Second,  
375 *process models* describe the spatial distribution of snow depth (i.e., snow depth field) as function  
376 of topography and correlation parameters. Finally, *prior models* define the prior information of  
377 parameters. The hierarchical approach breaks down a complex posterior distribution into a series  
378 of simple models, and hence enables us to capture complex relationships easily. In addition to  
379 the snow field vector and data vectors, two parameter vectors are defined: the process-model  
380 parameter vector  $\mathbf{a}$  to represent the heterogeneous pattern of snow depth, and the data-model  
381 parameter vector  $\mathbf{b}$  to describe the correlations between the snow depth and the GPR travel time.

382

383 We assume a linear model to describe the snow depth field,

$$384 \quad \mathbf{y} = \mathbf{A}\mathbf{a} + \boldsymbol{\tau} \quad (1)$$

385 where  $A$  is the design matrix as a function of the topographic metrics as explanatory variables  
386 (and hence a function of DEM  $z_d$ ). The process-model parameter vector  $\mathbf{a}$  describes the  
387 correlation between the topographic metrics and the snow depth field. We assume that the  
388 residual of this correlation  $\boldsymbol{\tau}$  represents the unexplained variability by the topographic metrics  
389 and that  $\boldsymbol{\tau}$  is spatially correlated. The residual term  $\boldsymbol{\tau}$  is described by a multivariate normal  
390 distribution with a covariance  $\Sigma$ , which is determined by a geostatistical analysis (Diggle and  
391 Ribeiro, 2007). Although we may include the uncertainty of those geostatistical parameters in the  
392 Bayesian estimation (Diggle and Ribeiro, 2007; Lavigne et al., 2016), we assume that those  
393 parameters are fixed during the Bayesian estimation process in this study. This is because we  
394 have a large amount of point measurements (snow depth probe data), and also it is known that  
395 indirect information (such as geophysics) does not significantly improve the estimation of  
396 geostatistical parameters (Day-Lewis, 2004; Murakami et al., 2010).

397

398 The data model for the snow depth probe measurements defines the snow depth probe data  $\mathbf{z}_p$  as  
399 a function of snow depth  $\mathbf{y}$ :

$$400 \quad \mathbf{z}_p = \mathbf{y} + \boldsymbol{\varepsilon}_p \quad (2)$$

401 We assume that the vector  $\boldsymbol{\varepsilon}_p$  is an uncorrelated normally-distributed measurement error at each  
402 data location with the standard deviation of  $\sigma_p$ . We determine the error based on the precision  
403 estimate of each snow depth probe. The snow depth probe data vector  $\mathbf{z}_p$  follows a multivariate  
404 normal distribution with the mean vector  $\mathbf{y}$  and the covariance matrix  $D_p$ , which is a diagonal  
405 matrix with diagonal elements of  $\sigma_p^2$ . Although it is not considered this study, we could include a  
406 systematic bias of snow probe measurements as an added shift (Berezovskaya and Kane, 2007).

407

408 The data model for the GPR data describes the GPR data  $\mathbf{z}_g$  as a function of the snow depth  $\mathbf{y}$  at  
 409 the GPR locations. The GPR data model can be represented by a linear model:

$$410 \quad \mathbf{z}_g = b_0 + \mathbf{B}\mathbf{y} + \boldsymbol{\varepsilon}_g \quad (3)$$

411 where  $\mathbf{B}$  is a matrix, the diagonal elements of which is  $b_1$ . The error vector  $\boldsymbol{\varepsilon}_g$  is an uncorrelated  
 412 normally-distributed measurement error with the standard deviation of  $\sigma_g$ . The standard  
 413 deviation is computed from comparing the GPR-based snow depth to the probe-based one. At the  
 414 same time, the GPR data model can be written as a function of the parameter vector  $\mathbf{b}$  such that:

$$415 \quad \mathbf{z}_g = \mathbf{Y}\mathbf{b} + \boldsymbol{\varepsilon}_g \quad (4)$$

416 where  $\mathbf{Y}$  is the design matrix with the first column being  $\mathbf{y}$ , and the second column being all one.

417 The parameter vector  $\mathbf{b} = \{b_1, b_0\}$  represents the linear correlations between the GPR data and  
 418 snow depth. This alternative model is useful during the estimation procedure described below.

419 The GPR data vector  $\mathbf{z}_g$  follows a multivariate normal distribution with the mean vector  $\mathbf{y}$  and the  
 420 covariance matrix  $\mathbf{D}_g$  that is a diagonal matrix with diagonal elements of  $\sigma_g^2$ .

421

422 The posterior distribution of the snow depth conditioned on the datasets  $p(\mathbf{y} | \mathbf{z}_d, \mathbf{z}_p, \mathbf{z}_g)$  is a  
 423 marginal distribution of  $p(\mathbf{y}, \mathbf{a}, \mathbf{b} | \mathbf{z}_d, \mathbf{z}_p, \mathbf{z}_g)$ . By applying Bayes's rule and following the  
 424 conditional dependencies defined above, we can decompose this posterior distribution as:

$$425 \quad p(\mathbf{y}, \mathbf{a}, \mathbf{b} | \mathbf{z}_d, \mathbf{z}_p, \mathbf{z}_g) \propto p(\mathbf{z}_g | \mathbf{y}, \mathbf{b}) p(\mathbf{z}_p | \mathbf{y}) p(\mathbf{y} | \mathbf{a}, \mathbf{z}_d) p(\mathbf{a}) p(\mathbf{b}). \quad (5)$$

426 Table 1 defines all the distributions on the right-hand side of Equation (5) based on the models  
 427 defined in Equations (1) – (4). We also assume multivariate normal distributions for the prior  
 428 distributions of the parameter vectors  $\mathbf{a}$  and  $\mathbf{b}$ . The posterior distribution in Equation (5) can be  
 429 computed using the Markov-chain Monte-Carlo (MCMC) method (Gamerman and Lopes, 2006).

430 Since all the distributions are defined as multivariate normal distributions, it is possible to use

431 efficient Gibbs' algorithm. The MCMC procedure is described in Appendix A. The convergence  
432 can be confirmed by the Geweke's convergence diagnostic (Geweke, 1992). The entire workflow  
433 is included in Appendix B.

434 **4. Results**

435 **4.1. Snow Depth Measurements**

436 *GPR Radar Velocity Analysis*

437 Our results (based on the GPR data and tile probe data collected in May 2012) indicate that the  
438 estimated radar velocity itself does not have a systematic dependency on (or trend with) the snow  
439 depth or submeter-scale variability of topography in May 2012 (Figures 2a and 2b). The  
440 correlation coefficient between the radar velocity and snow depth is 0.11, and between the radar  
441 velocity and submeter-scale variability is 0.15. The variability of the radar velocity, on the other  
442 hand, depends on those two factors (i.e., the variability of snow depth and topography). Hence,  
443 the variability is higher in areas with shallower snow depths (Figure 2a). The standard deviation  
444 (STDEV) of the radar velocity is 0.039 m/ns at the snow depth smaller than one STDEV minus  
445 the median snow depth, and 0.019 m/ns at the one larger than one STDEV plus the median. The  
446 radar velocity variability is higher also in localized regions of large submeter-scale topographic  
447 variability (Figure 2b). The STDV of the radar velocity is 0.015 m/ns at the submeter-scale  
448 topographic variability (i.e. elevation difference within a one-meter radius) smaller than 0.05 m,  
449 and 0.036 m/ns at the one larger than 0.05m. By selecting the points with the submeter-scale  
450 topographic variability < 0.05 m, we obtained a mean radar velocity of 0.25 m/ns, which was  
451 used for subsequent analysis.

452

453 Using the mean velocity value in May 2012, the calculated GPR-based snow depth estimates  
454 were compared with the snow depth probe measurements (Figure 2c). The correlation between  
455 the measured and estimated snow depth is high (the correlation coefficient is 0.88), with the root  
456 mean square error (RMSE) being 5.4 cm, and with no significant under- or overestimation (the

457 mean bias error  $-0.16$  cm). The selected points in the regions of low submeter-scale topographic  
458 variability (red circles) are more tightly distributed around the one-to-one line. In these regions,  
459 the RMSE of GPR-based snow depth improved to  $2.9$  cm with a increased correlation coefficient  
460 between the GPR-based and probe-based snow depth to  $0.94$ . These results confirm that snow  
461 density variations are limited, and using a constant mean GPR velocity is acceptable.

462

### 463 *Snow Depth Measurements in Different Polygon Types*

464 Figure 3 shows the LiDAR DEM as well as snow depth probe measurements and GPR estimates  
465 in Plots A–D (May 2012). The LiDAR DEM (in the left column) illustrates the difference among  
466 four plots in terms of both macro- and microtopography. For example, Plot A has better defined  
467 polygon rims and troughs than Plot D, although Plot A and D are both low-centered polygons.  
468 Plot B has round-shaped high-centered polygons, while Plot C has flat-centered polygons with  
469 well-defined troughs. The average size of polygons is also different, with smaller polygons in  
470 Plot B and larger polygons in Plots A, C and D. In addition, these figures illustrate some  
471 macrotopographic trends. Plot C is gradually sloping down towards the east, and Plot D has a  
472 depression (i.e., DTLB) in the northeastern half.

473

474 The middle column in Figure 3 shows the snow depth probe data collected using the fine-grid  
475 and coarse-grid scheme collected in May 2012. The fine-grid data reveals the detailed  
476 heterogeneity of snow depth around a single polygon. For example, the fine-grid data in Plot A  
477 show the snow depth distribution in a low-centered polygon, including thin snow along the  
478 polygon rim and thick snow at the polygon center and trough. Comparison of the fine-grid snow  
479 data with the DEM reveals the microtopographic effect such that the troughs and center of the

480 polygon have larger snow depth. The coarse-grid dataset covers the entire plot, although it is  
481 much more difficult to ascertain the relationship between the snow depth and microtopography.  
482 The snow depth probe data show that the snow depth is highly variable, ranging from 0.2 m to  
483 0.8 m in a single plot.

484

485 In the third column of Figure 3, the May-2012 snow depth was estimated from GPR using a  
486 fixed radar velocity 0.25 m/ns along the lines within the plots, and then interpolated with a  
487 simple linear interpolation in between the lines. The high-resolution GPR snow depth estimates  
488 are useful for determining if microtopographic features can influence the distribution of snow  
489 depths across each study plot.. The high-resolution snow estimates over the large area allow us to  
490 visually identify the macrotopographic control on snow depth. In Plot C, for example, the snow  
491 depth does not have an increasing or decreasing trend, even though the elevation gradually  
492 decreases towards east. Plot D, on the other hand, has more snow accumulation in the eastern  
493 part of the domain, which is in the depression associated with DTLB.

494

#### 495 *PhoDAR-based Snow Depth Measurements*

496 In the region of the 500-meter transects, the PhoDAR-derived snow-free DSMs (Figure 4a)  
497 collected in July 2013 and August 2014 were first compared with the RTK DGPS data (acquired  
498 in 2011) in Table 2, using the different schemes to identify co-location. We included the results  
499 of both years to confirm the consistency between the two snow-free DSM products at the same  
500 terrain. Although all the scheme yielded an excellent accuracy (the RMSE less than 7.0 cm),  
501 taking the average provides the lowest RMSE in both years (6.41 cm in 2013 and 6.19 cm in  
502 2014), which is approximately the same as the LiDAR data (RMSE = 6.08 cm). The PhoDAR-

503 derived snow depth estimates in May 2015 were obtained by differencing the snow surface and  
504 snow-free DSM (Figure 4b). The comparison between the PhoDAR-based snow estimates and  
505 the snow depth probe data are favorable (Figure 4c), with a RMSE of 6.0 cm. When we removed  
506 the points that had a large submeter-scale topographic variability in the vicinity (in the same way  
507 and the same cut-off values as the GPR snow depth analysis), the RMSE improved to 4.6 cm  
508 (Figure 4c).

509

510 The PhoDAR-derived snow depth (Figure 4b) around the 500-meter transects in May 2015  
511 reveals a similar pattern of snow distribution as the GPR data in Figure 3, having deeper snow in  
512 the troughs and the centers of low-centered polygons. The high-resolution image of the PhoDAR  
513 data reveals more detail of the microtopographic effect than the interpolated image of the GPR  
514 data, particularly in the narrow troughs. The large aerial coverage also shows the minimal effect  
515 of macrotopography: while the elevation decreases towards south, the snow depth does not have  
516 a large-scale trend.

517

## 518 **4.2. Snow Depth Variability over Tundra**

### 519 *Variability among Different Polygon Types*

520 Figure 5 shows the boxplots of the snow depth, elevation, and microtopographic elevation  
521 ( $\Delta$ elevation) in each plot measured in May 2012. We used the coarse-grid snow depth probe  
522 measurements, since the samples are uniformly distributed over each plot. The median snow  
523 depth (Figure 5a) is fairly similar among four plots, even though they have different  
524 geomorphologic features and polygon types. Tukey's pairwise comparison test (Table 3) shows  
525 that only Plot B (small high-centered polygons) is significantly different from the other plots.

526

527 The absolute elevation distribution varies among the four plots (Figure 5b), although the snow  
528 depth for each of the plots has similar median values and distributions. Plot A (well-defined low-  
529 centered polygons), for example, is at a higher elevation than Plots C (flat-centered polygons)  
530 and D (low-centered polygons in DTLB), but the difference in the average snow depth is not  
531 statistically significant (Table 3). The microtopographic elevation is computed based on the  
532 wavelet transform with the scale of 32 m as described in Section 3.3 (Figure 5b). The scale of 32  
533 m was selected to yield the best correlation between snow depth and microtopographic elevation.  
534 Plot D (low-centered polygons in DTLB), for example, has less variability in both elevation and  
535 snow depth, because Plot D has less distinct microtopography than others. In contrast, Plot B has  
536 the largest variability in both microtopography and snow depth

537

### 538 *Correlations between Snow Depth and Topographic Indices in May 2012*

539 Among the topographic indices of macro- and microtopography, the snow depth in May 2012  
540 (measured by the snow depth probe) was significantly correlated only to the microtopographic  
541 elevation for all plots (Figure 6a). The correlation coefficient changes with the scale of the  
542 wavelet transform that separates micro- and macrotopography. The correlation coefficient is up  
543 to  $-0.8$  at Plot B (small high-centered polygons), and up to  $-0.7$  at all the data points. The  
544 correlation coefficient is different among different plots (i.e., different polygon types); the  
545 correlation is less significant at Plot D (low-centered polygons in DTLB), than other plots. The  
546 best correlation (i.e., the largest absolute value) can be achieved at a different scale in each plot  
547 (Plot B < Plot A and Plot C < Plot D).

548

549 A significant correlation between snow depth and wind factor of macrotopography was identified  
550 only in Plot D (low-centered polygons in DTLB; Figure 6b). The correlation coefficient is up to  
551 0.41 at the scale of 38 m. Other topographic indices (i.e., the slope and curvature of both micro-  
552 and macrotopography, the wind factor of microtopography) are not shown here, since we did not  
553 find any significant correlation. Although Dvornikov et al. (2015) reported a strong correlation  
554 between snow depth and curvature (snow free DEM), we did not find any significant correlation  
555 in our data. This is possibly because the microtopography at our site was completely filled by  
556 snow, and the overall elevation gradient at our site (the elevation difference in the domain is 3.1  
557 m) is much smaller than the one that Dvornikov et al. (2015) reported (the elevation difference in  
558 their domain was more than 60 m).

559

### 560 *Geostatistical Analysis of Snow Depth*

561 Spatial correlation exists for all three variables in May 2012: snow depth, snow surface, and  
562 residual snow depth after removing the correlation to the microtopographic elevation (Table 4).  
563 The correlation range is less than 20 m for the snow depth, which is consistent with the large  
564 variability in a short distance. The snow surface, on the other hand, has a larger correlation range  
565 (253 m). The estimation of a snow surface height (elevation + snow depth), effectively removes  
566 the influence of microtopography, resulting in much a larger correlation range. The variance is  
567 comparable between the snow depth and snow surface, while the variance is much lower in the  
568 residual snow depth, since the topographic correlation explains a large portion of the snow depth  
569 variability.

570

### 571 **4.3. Snow Depth Estimation based on LiDAR DEM**

572 Based on the snow-topography analysis in Section 4.2, we included the linear correlation  
573 between snow and microtopographic elevation in Equation (1), to describe the snow variability  
574 in May 2012. We used the Shapiro-Wilk normality test to confirm that the residual of the linear  
575 correlation, defined by  $\tau$  in Equation (1), follows a normal distribution (the p-value of rejecting  
576 this hypothesis was 0.21). The first column of the design matrix  $A$  is the microtopographic  
577 elevation at all the pixels, and the second one is a vector of all ones. The parameter vector  $\mathbf{a}$  is a  
578 2-by-1 vector with the linear correlation parameters (slope and intercept). The Bayesian method  
579 (Section 3.4) yielded 10,000 equally likely fields of the snow depth from the posterior  
580 distribution in Equation (5).

581

582 The Bayesian estimated mean snow-depth field over the full study domain in May 2012 (Figure  
583 7a) captures the effects of microtopography, such as more snow accumulation in polygon troughs  
584 and centers of low-centered polygons. The snow depth does not have any large-scale trends over  
585 the full study domain, which is different from the LiDAR DEM in Figure 1b, but consistent with  
586 the interpolated GPR snow depths depicted in Figure 3 (right column), and the measured UAS  
587 snow depth measurements depicted in Figure 4b. The variability is larger in the southern region  
588 where there are high-centered polygons with deep troughs.

589

590 In addition, we compared this result (Figure 7a) with the mean field by estimating the snow  
591 surface elevation and subtracting the ground surface elevation (Figure 7b). In this estimation, we  
592 used the same Bayesian algorithm one described in Section 3.4, except that we removed the  
593 topographic correlations and assumed a standard geostatistical model for snow surface (Diggle  
594 and Ribeiro, 2007). In other words, we had the same algorithm except that we modified Equation

595 (1) to  $y = -z + \tau$ , where  $y + z$  represents the surface elevation. Although the two mean fields  
596 (Figure 7) are similar in the central regions that have many measurements, the regions without  
597 any measures have a significant deviation. This is because the snow surface estimation did not  
598 capture the change in macrotopography (e.g. the drainage feature in the southern part of the  
599 domain).

600

601 The estimated standard deviation of the Bayesian-derived snow depth over the study domain  
602 (Figure 8a) also shows a significant difference from the one based on the snow surface  
603 interpolation (Figure 8b). This standard deviation represents the uncertainty in the estimation. In  
604 both cases, the standard deviation is smaller near the measurement locations along the transects  
605 and within the four plots. However, when the topographic correlation is included (Figure 8a), the  
606 standard deviation increases more rapidly as the pixel is farther away from the data points. This  
607 is due to the fact that the spatial correlation range is small for the residual snow depth after  
608 removing the topographic correlation (Table 4).

609

610 Validation of the snow depth estimates over the study area (Plot A-D and the 500-meter  
611 transects) was performed by comparing the estimates with the snow depth probe data (May  
612 2012) not used in the Bayesian snow depth estimation. We selected 100 points randomly from  
613 the snow depth probe data (all the locations in Plot A-D and the 500-meter transects), using a  
614 uniform distribution. The validation results (Figure 9) show that the estimated confidence  
615 interval captures the probe-measured snow depth. The estimated snow depth is distributed along  
616 with the one-to-one line without any significant bias. The estimation, including the topographic  
617 correlation (Figure 9a), has a tighter confidence interval and better estimation results than the

618 one from interpolating the snow surface (Figure 9b). The RMSE for the Bayesian method of  
619 estimating snow depth including the topographic correlation is 6.0 cm, while the RMSE for the  
620 interpolated snow surface is 8.8 cm.

621

622 **5. Discussion**

623 **5.1. Different Observational Platforms**

624 Our analysis showed that GPR data provided the end-of-winter snow depth distribution with high  
625 accuracy (RMSE = 2.9 cm) and resolution (10 cm along each line). The GPR-based estimation  
626 requires care, particularly regarding the estimation of radar velocity and associated possible  
627 errors, such as those due to positioning. Although the radar velocity is known to depend on the  
628 snow density, we attribute the variability of radar velocity at our site to random or positioning  
629 errors. Three results support this claim. First, the variability of radar velocity is smaller in a  
630 thicker snow pack, suggesting the small contribution of the error relative to the overall snow  
631 depth. The relatively low topographic variability over the site (compared to mountainous  
632 terrains) would have contributed to this fairly uniform radar velocity. Second, the radar velocity  
633 variability depends on the submeter-scale variability of the topography in the vicinity of the  
634 calibration points, suggesting the impact of positioning errors. Third, there was no systematic  
635 trend in the radar velocity as a function of the snow depth or topographic positions. We  
636 developed a simple methodology (described in Section 3.1) to select co-located calibration points  
637 based on the submeter-scale variability of topography, which proved to be useful to compute  
638 accurate velocity. We note that – even though the depth-averaged radar velocity and hence the  
639 depth-averaged snow density have little variability over the space –the snow density could be  
640 variable vertically along the depth. From snow coring, we indeed found some layers of ice  
641 created by winter rain events that were not detected by the GPR or with probe. It is possible that  
642 there might be a difference in the depth-averaged density and radar velocity at a later time, when  
643 the snow pack starts to melt in a heterogeneous manner.

644

645 UAS-based PhoDAR provided an attractive alternative for estimating snow depth at high  
646 resolution over a large area. With much less labor and time, UAS-based PhoDAR can provide  
647 many more sample points than GPR. The PhoDAR-based snow depth, however, was less  
648 accurate than ground-based GPR or snow depth probe measurements (RMSE = 6.0 cm). The  
649 main contribution of this error resulted from the snow-free elevation, since RMSE for the surface  
650 DSM is around 6 cm. We note that the RMSE of 6.0 cm is still significantly more accurate than  
651 the previous LiDAR and other airborne surveys (e.g., Deems et al., 2013; Harpold et al. 2014;  
652 Nolan et al., 2015).

653  
654 The PhoDAR-based approach is expected to continue its trajectory of continuous improvements  
655 in terms of technical aspects, ease of use, and accuracy. At the time of our campaign, we were  
656 allowed to use only a kite due to regulations, which led to a limited number of pictures that could  
657 be used to reconstruct the DSM. The accuracy will significantly improve with the use of a light  
658 unmanned aerial vehicle (UAV). Although UAS-based LiDAR acquisition technology continues  
659 to improve (e.g., Anderson and Gaston, 2013), as is expected to be a powerful alternative to  
660 characterize snow, the LiDAR device is still significantly more expensive than a conventional  
661 camera (roughly by factor of 100). Given that the vegetation height is fairly small in the Arctic  
662 tundra, the PhoDAR technique is an affordable alternative.

663  
664 For all the types of measurements, accurate positioning was critical in the polygonal tundra due  
665 to microtopography. The GPS snow depth probe (Snow-Hydro), for example, had the positioning  
666 error larger than several meters, and required extra post-processing to correct the locations. On  
667 the other hand, measuring the RTK DGPS at all the snow depth measurement locations would

668 not be realistic since it would take time. We found that having a measurement tape and  
669 measuring the start and end points by the DGPS were a reasonable approach, when the snow  
670 surface is smooth and hard. In this study, we used the snow depth probe data as the true snow  
671 depth to compare with other measurements (i.e., GPR, PhoDAR, and Bayesian estimation). To  
672 improve the accuracy further, it would be necessary to quantify the uncertainty in the snow depth  
673 probe associated with the vegetation and other issues (Berezovskaya and Kane, 2007).

674

## 675 **5.2. Snow Depth Variability**

676 The end-of-year snow depth distribution at the ice-wedge polygons was highly variable over a  
677 short distance in May 2012. The snow depth was, however, significantly correlated with the  
678 microtopographic elevation, suggesting that the snow depth could be described by  
679 microtopography. The wind-blown snow transport leads to significant snow redistribution, and  
680 fills microtopographic lows (i.e., troughs and centers of low-centered polygons) with thicker  
681 snow pack (e.g., Pomeroy et al., 1993). The redistribution also results in the smooth snow  
682 surface, following the macrotopography. The exception was observed at the edge of the DTLB,  
683 where the abrupt change in macrotopography led to increased accumulation in the depression.  
684 This is a similar effect to that observed along the riverbanks by Benson and Sturm (1993).  
685 Although the tundra ecosystem studies have focused on the effect of microtopography (e.g.,  
686 Zona et al., 2011), the macrotopography also may be important when we characterize snow  
687 distribution over a larger area.

688

689 The “average” (or median) snow depth over a hundred-meter scale (i.e., the size of Plots A-D),  
690 on the other hand, was fairly uniform across the site despite the different polygon types in May

691 2012. Plot A (well-defined low-centered polygons) and C (flat-centered polygons), for example,  
692 have different polygon types, but they have a similar median snow depth. This is because  
693 microtopography and microtopographic features (i.e., polygon troughs, rims) mainly control the  
694 snow distribution. Plot B (small high-centered polygons) is an exception, having smaller median  
695 snow depth than the other plots. Plot B has the largest variability in microtopography,  
696 characterized by the small round high-centered polygons, like numerous small mounds (Figure  
697 3). Such mounds are prone to erosion by the wind, and hence lead to less snow trapping and  
698 accumulation.

699

700 Identifying such correlations between snow depth and topography requires an effective approach  
701 to separate micro- and macrotopography. Our wavelet analysis revealed that the separation scale  
702 depends on the polygon sizes; for example, the larger polygons in Plot A (well-defined low-  
703 centered polygons) and C (flat-centered polygons) lead to a larger separation scale than the  
704 smaller polygons in Plot B (small high-centered polygons). It is a challenge to map  
705 macrotopography accurately over a larger area, particularly at the present site, where different  
706 types and sizes of polygons mix. Although we used the same scale for the estimation, an  
707 improved polygon delineation algorithm will possibly enable us to separate micro- and  
708 macrotopography in the future (e.g., Wainwright et al., 2015).

709

### 710 **5.3. Snow Depth Estimation**

711 The developed Bayesian approach enabled us to estimate the snow depth distribution over a large  
712 area based on the LiDAR DEM and the correlation between the snow depth and topography.  
713 Although this paper only used the ground-based GPR and snow depth probe measurements

714 collected at the same time, PhoDAR could be easily included in the same framework. The  
715 Bayesian method allowed us to integrate three types of datasets (LiDAR DEM, snow depth  
716 probe and GPR) in a consistent manner, and also provided the uncertainty estimate for the  
717 estimated snow depth. Taking into account the topographic correlation explicitly improved the  
718 accuracy of estimation significantly (RMSE 6.0 cm), compared to interpolating the snow surface  
719 and subtracting the DEM (RMSE 8.8 cm).

720

721 Our approach can be extended to snow estimates over both time and space. The correlations  
722 between snow depth and topography may change over time. In early and later winter, for  
723 example, the snow depth would be more affected by curvature and slope of microtopography,  
724 since the microtopographic lows (troughs and centers of the low-centered polygons) are not  
725 filled by snow. It would be possible to quantify the seasonal changes in the topography-snow  
726 correlations by designing a full season ground-based measurement campaign and acquisition of  
727 remote sensing snow depth measurements (by PhoDAR or LiDAR), that monitored the same site  
728 over several years to account for inter-annual variability. The Bayesian method presented here is  
729 flexible enough to account for changes in parameters over time for the spatial-temporal data  
730 integration (e.g., Wikle et al., 2001). Although physically-based snow distribution models can be  
731 used for the same purposes (e.g., Pomeroy et al., 1993; Liston and Sturm, 1998; 2002), it is  
732 difficult to parameterize all the processes, such as sublimation and turbulent transport. Our data-  
733 driven approach provides a powerful alternative to distribute snow depth based on various  
734 datasets.

735 **6. Summary**

736 In this study, we explored various strategies to estimate the end-of-year snow depth distribution  
737 over an Arctic ice-wedge polygon tundra region. We first developed an effective methodology to  
738 calibrate GPR and PhoDAR in the presence of submeter-scale-scale variability of topography.  
739 We then investigated the characteristics and accuracy of three observational platforms: snow  
740 depth probe, GPR and PhoDAR. The PhoDAR-derived snow depth estimates have great  
741 potential for accurately characterizing snow depth over larger regions (with an RMSE of 4.6 cm),  
742 relative to the in situ snow depth measurements. The GPR snow depth estimates were slightly  
743 more accurate (with an RMSE of 2.9 cm), but required considerable more effort to obtain, and  
744 require complex post-processing to minimize errors associated with radar positioning.

745  
746 We investigated the spatial variability of the snow depth and its dependency on the topographic  
747 metrics. At the peak snow depth during our data acquisition, the snow depth was highly  
748 correlated with microtopographic elevation (the correlation coefficient of up to  $-0.8$ ), although it  
749 was highly variable over short distances (the correlation range of 12.3 m). It is considered that  
750 the wind redistribution filled the microtopography by snow, and created a snow surface  
751 following macrotopography at the site. The challenge was to separate macro- and  
752 microtopography, since the separation scale was not arbitrary, and depended on the polygon size.  
753 The wavelet analysis provided an effective approach to identify this separation scale.

754  
755 The Bayesian method was effective at integrating different measurements to estimate snow depth  
756 distribution over the site. Although our estimation is based on the data collected from a one-time  
757 campaign, and the correlations to topography may change over time, the approach developed

758 here is expected to be applicable for estimating both spatial and temporal variability of snow  
759 depth at other sites, and in other landscapes..

760

761 **Appendix A**

762 In MCMC, we sample each variable sequentially conditioned on all the other variables. In other  
763 words, when we update one variable (or one vector), we assume that the other variables are  
764 known and fixed. After sampling thousands of sets of the variables, the distribution of those  
765 samples converges to the posterior distribution. Each vector is sampled as follows:

766

767 The snow depth field is sampled from the distribution:

768 
$$p(\mathbf{y} | \bullet) = p(\mathbf{y} | \mathbf{a}, \mathbf{b}, \mathbf{z}_d, \mathbf{z}_g, \mathbf{z}_p) \propto p(\mathbf{z}_g | \mathbf{y}, \mathbf{b}) p(\mathbf{z}_p | \mathbf{y}) p(\mathbf{y} | \mathbf{a}, \mathbf{z}_d) \quad (\text{A.1})$$

769 where “•” represents all the other variables. The distribution is decomposed to a series of small  
770 conditional distributions defined in Table 1. Similarly, we can sample the snow-process  
771 parameters  $\mathbf{a}$  and GPR-data parameter  $\mathbf{b}$  from the distributions:

772 
$$p(\mathbf{a} | \bullet) = p(\mathbf{a} | \mathbf{y}, \mathbf{h}) \propto p(\mathbf{y} | \mathbf{h}, \mathbf{a}) p(\mathbf{a}) \quad (\text{A.2})$$

773 
$$p(\mathbf{b} | \bullet) = p(\mathbf{b} | \mathbf{y}, \mathbf{z}_g) \propto p(\mathbf{z}_g | \mathbf{y}, \mathbf{b}) p(\mathbf{b}) \quad (\text{A.3})$$

774 Since all the distributions in Equation A.1–A.3 are multivariate Gaussian, we can use the  
775 conjugate prior to compute an analytical form of each distribution. Each distribution is  
776 multivariate Gaussian with the covariance and mean vector defined in Table A.1. In the Gibbs’  
777 sampling algorithm, we sample each variable vector sequentially until the distributions are  
778 converged.

779

780 **Appendix B**

781 The workflow of the Bayesian geostatistical approach from the data is included in Figure B.1.

782 The snow depth probe data and LiDAR DEM are used to (a) identify the correlations between

783 topography and snow depth (Section 3.3) after identifying the representative scale of macro- and

784 micro-topography in the wavelet analysis, to (b) quantify the variogram parameters, and also to  
785 (c) create a process model in Equation (1). The GPR data are analyzed to estimate the radar  
786 velocity, and to quantify the correlations to the snow depth probe (Section 3.1). At the end (the  
787 last column in Figure B.1), all the parameters are assembled for the estimation using MCMC  
788 (Appendix A).

789

790

791 **Acknowledgements**

792 The Next-Generation Ecosystem Experiments (NGEE) Arctic project is supported by the Office  
793 of Biological and Environmental Research in the DOE Office of Science. This NGEE-Arctic  
794 research is supported through contract number DE-AC0205CH11231 to Lawrence Berkeley  
795 National Laboratory. We gratefully acknowledge Stan Wullschleger in Oak Ridge National  
796 Laboratory, project PI. We thank Dr. Craig Tweedie at University of Texas, El Paso for  
797 providing the LiDAR dataset, and together with Sergio Vargas from University of Texas, El  
798 Paso, for providing kite-based landscape imaging advice. Datasets are available upon request by  
799 contacting the corresponding author (Haruko M. Wainwright, [hmwainwright@lbl.gov](mailto:hmwainwright@lbl.gov)).

800

801 **Reference:**

- 802 Anderson, B. T., McNamara, J. P., Marshall, H. P., & Flores, A. N. (2014). Insights into the  
803 physical processes controlling correlations between snow distribution and terrain properties.  
804 *Water Resources Research*, 50(6), 4545-4563.
- 805 Anderson, K., and Gaston, K. J. (2013). Lightweight unmanned aerial vehicles will revolutionize  
806 spatial ecology. *Frontiers in Ecology and the Environment*, 11(3), 138-146.
- 807 Annan, A.P., 2005, Ground penetrating radar, in near surface geophysics, in D.K. Butler (eds),  
808 Society of Exploration Geophysicists, Tulsa, OK, USA, Investigations in Geophysics No. 13,  
809 pp. 357–438.
- 810 Benson, C. S., and Sturm, M. (1993). Structure and wind transport of seasonal snow on the  
811 Arctic slope of Alaska. *Annals of Glaciology*, 18, 261-267.
- 812 Berezovskaya S, Kane DL. 2007. Measuring snow water equivalent for hydrological  
813 applications: part 1, accuracy of observations. In: Proceedings of the 16th International  
814 Northern Research Basins Symposium and Workshop. Petrozavodsk, Russia  
815 [http://resources.krc.karelia.ru/krc/doc/publ2007/SYMPOSIUM\\_029-35.pdf](http://resources.krc.karelia.ru/krc/doc/publ2007/SYMPOSIUM_029-35.pdf)
- 816 Binley, A., Hubbard, S.S., Huisman, J., Revil, A., Robinson, D., Singha, K., and Slater, L. (2015)  
817 The emergence of hydrogeophysics for improved understanding of subsurface processes over  
818 multiple scales. DOI: 10.1002/20015WR017016
- 819 Bowling, L. C., D. L. Kane, R. E. Gieck, L. D. Hinzman, and D. P. Lettenmaier, The role of  
820 surface storage in a low-gradient Arctic watershed, *Water Resour. Res.*, 39(4), 1087,  
821 doi:10.1029/2002WR001466, 2003.
- 822 Bjørke, J. T., and Nilsen, S. (2003). Wavelets applied to simplification of digital terrain models.  
823 *International Journal of Geographical Information Science*, 17(7), 601-621.

824 Brown, J. (1967), Tundra soils formed over ice wedges, northern Alaska, *Soil Sci. Soc. Am. J.*,  
825 31(5), 686–691

826 Callaghan, T. V., M. Johansson, R.D. Brown, P. Y. Groisman, N. Labba, V. Radionov, R.S.  
827 Bradley, S. Blangy, O.N. Bulygina, T.R. Christensen, J.E. Colman, R.L.H. Essery, B.C.  
828 Forbes, M.C. Forchhammer, V.N. Golubev, R. E. Honrath, G.P. Juday, A.V. Meshcherskaya,  
829 G.K. Phoenix, J. Pomeroy, A. Rautio, D.A. Robinson, N.M. Schmidt, M.C. Serreze, V.P.  
830 Shevchenko, A.I. Shiklomanov, A.B. Shmakin, P. Sköld, M. Sturm, M. Woo, E. F. Wood,  
831 (2011). Multiple Effects of Changes in Arctic Snow Cover. *Ambio*, 40 (Suppl 1), 32–45.  
832 Doi:10.1007/s13280-011-0213-x.

833 Clein, J. S., & Schimel, J. P. (1995). Microbial activity of tundra and taiga soils at sub-zero  
834 temperatures. *Soil Biology and Biochemistry*, 27(9), 1231-1234.

835 Dafflon, B., Hubbard, S., Ulrich, C., Peterson, J., Wu, Y., Wainwright, H., & Kneafsey, T. J.  
836 (2016). Geophysical estimation of shallow permafrost distribution and properties in an ice-  
837 wedge polygon-dominated Arctic tundra region. *Geophysics*, 81(1), WA247-WA263.

838 Davison, A. C. (2003). *Statistical models* (Vol. 11). Cambridge University Press.

839 Deems, J. S., Painter, T. H., & Finnegan, D. C. (2013). Lidar measurement of snow depth: a  
840 review. *Journal of Glaciology*, 59(215), 467-479.

841 Day-Lewis, F. D., and J. W. Lane Jr. (2004), Assessing the resolution-dependent utility of  
842 tomograms for geostatistics, *Geophys. Res. Lett.*, 31, L07503, doi:10.1029/2004GL019617.

843 Derksen, C., A. Silis, M. Sturm, J. Holmgren, G. Liston, H. Huntington, and D. Solie, 2009:  
844 Northwest Territories and Nunavut Snow Characteristics from a Subarctic Traverse:  
845 Implications for Passive Microwave Remote Sensing. *J. Hydrometeor.*, 10, 448–463, doi:  
846 10.1175/2008JHM1074.1.

847 Diggle, P. and Ribeiro, P. J. (2007). Model-based geostatistics. Springer Science & Business  
848 Media.

849 Dvornikov, Y., Khomutov, Mullanurov, and Ermokhina (2015), GIS- and field data based  
850 modeling of snow water equivalent in shrub tundra, *Ice and Snow*, doi:10.15356/2076-6734-  
851 2015-2-69-80.

852 Engstrom, R., Hope, A., Kwon, H., Stow, D., & Zamolodchikov, D. (2005). Spatial distribution  
853 of near surface soil moisture and its relationship to microtopography in the Alaskan Arctic  
854 coastal plain. *Hydrology Research*, 36(3), 219-234.

855 Gamerman, D. and H. F. Lopes (2006), Markov Chain Monte Carlo – Stochastic simulation for  
856 Bayesian inference. Chapman&Hall/CRC, 2<sup>nd</sup> edition, Boca Raton, USA.

857 Gamon, J. A., G. P. Kershaw, S. Williamson, and D. S. Hik (2012), Microtopographic patterns in  
858 an arctic baydjarakh field: do fine-grain patterns enforce landscape stability? *Environ. Res.*  
859 *Lett.*, 7(1), 015502.

860 Geweke, J. (1992), Evaluating the accuracy of sampling-based approaches to calculating  
861 posterior moments, in *Bayesian Statistics 4* (edited by J. M. Bernardo, J. O. Berger, A. P.  
862 Dawid and A. F. M. Smith), Clarendon Press, Oxford, UK.

863 Gillin, C., S. Bailey, K. McGuire, and J. Gannon (2015), Mapping of Hydropedologic Spatial  
864 Patterns in a Steep Headwater Catchment, *Soil Science Society of America Journal*, 79(2),  
865 440, doi:10.2136/sssaj2014.05.0189.

866 Gusmeroli, A., and Grosse, G. (2012). Ground penetrating radar detection of subsnow slush on  
867 ice-covered lakes in interior Alaska. *The Cryosphere*, 6(6), 1435-1443.

868 Gusmeroli, A., G. Wolken, and A. Arendt (2014), Helicopter-borne radar imaging of snow cover  
869 on and around glaciers in Alaska, *Annals of Glaciology*, 55(67), 78–88,  
870 doi:10.3189/2014aog67a029.

871 Harper, JT, and JH Bradford (2003), Snow stratigraphy over a uniform depositional surface:  
872 spatial variability and measurement tools, *Cold Regions Science and Technology*.

873 Harpold, A. A., et al. (2014), LiDAR-derived snowpack data sets from mixed conifer forests  
874 across the Western United States, *Water Resour. Res.*, 50, doi:10.1002/2013WR013935.

875 Hinkel, K. M., W. R. Eisner, J. G. Bockheim, F. E. Nelson, K. M. Peterson, and X. Dai (2003),  
876 Spatial extent, age, and carbon stocks in drained thaw lake basins on the Barrow Peninsula,  
877 Alaska, *Arct., Antarct., and Alp. Res.*, 35(3), 291-300.

878 Hirashima, H., Y. Kodama, N. Sato, T. Ohata, H. Yabuki, and A. Georgiadi, 2004: Nonuniform  
879 Distribution of Tundra Snow Cover in Eastern Siberia. *J. Hydrometeor.*, 5, 373–389, doi:  
880 10.1175/1525-7541(2004)005<0373:NDOTSC>2.0.CO;2.

881 Hubbard, S. and Y. Rubin (2005), Hydrogeophysics, Chapter 1 in *Hydrogeophysics*, Eds. Y.  
882 Rubin and S. Hubbard, Elsevier.

883 Hubbard, S. S., C. Gangodagamage, B. Dafflon, H. Wainwright, J. E. Peterson, A. Gusmeroli, C.  
884 Ulrich, Y. Wu, C. Wilson, C., J. Rowland, C. Tweedie, and S. D. Wulschleger (2013),  
885 Quantifying and relating land-surface and subsurface variability in permafrost environments  
886 using LiDAR and surface geophysical datasets, *Hydrogeol. J.*, 21(1), 149-169.

887 Jansson, JK, and N Taş (2014), The microbial ecology of permafrost, *Nature Reviews*  
888 *Microbiology*, doi:10.1038/nrmicro3262.

889 Jol., H.M., (2009), *Ground Penetrating Radar Theory and Applications*, Elsevier Science.

890 Kane, D. L., L. D. Hinzman, C. S. Benson, and G. E. Liston (1991), Snow hydrology of a  
891 headwater Arctic basin: 1. Physical measurements and process studies, *Water Resour. Res.*,  
892 27(6), 1099–1109, doi:10.1029/91WR00262.

893 Kalbermatten, M. (2010). Multiscale analysis of high resolution digital elevation models using  
894 the wavelet transform, Thesis, Ecole Polytechnique Federale de Lausanne.

895 Kalbermatten, M., Van De Ville, D., Turberg, P., Tuia, D., & Joost, S. (2012). Multiscale  
896 analysis of geomorphological and geological features in high resolution digital elevation  
897 models using the wavelet transform. *Geomorphology*, 138(1), 352-363.

898 Leffingwell, E. D. K. (1915), Ground-ice wedges: The dominant form of ground-ice on the north  
899 coast of Alaska, *J. Geol.*, 635-654.

900 Liljedahl, A. K., Hinzman, L. D., Harazono, Y., Zona, D., Tweedie, C. E., Hollister, R. D.,  
901 Engstrom, R., and Oechel, W. C. (2011) Nonlinear controls on evapotranspiration in arctic  
902 coastal wetlands, *Biogeosciences*, 8, 3375-3389, doi:10.5194/bg-8-3375-2011.

903 Liljedahl, A. K., Boike, J., Daanen, R. P., Fedorov, A. N., Frost, G. V., Grosse, G., ... &  
904 Necsoiu, M. (2016). Pan-Arctic ice-wedge degradation in warming permafrost and its  
905 influence on tundra hydrology. *Nature Geoscience*.

906 Liston, G. E., and Sturm, M. (1998). A snow-transport model for complex terrain. *Journal of*  
907 *Glaciology*, 44(148), 498-516.

908 Liston, G., and Sturm, M. (2002). Winter precipitation patterns in arctic Alaska determined from  
909 a blowing-snow model and snow-depth observations. *Journal of Hydrometeorology*, 3, 646–  
910 659.

911 MacKay, J. R. (2000), Thermally induced movements in ice-wedge polygons, western Arctic  
912 coast: a long-term study, *Géographie physique et Quaternaire*, 54(1), 41-68.

913 Machguth, H., O. Eisen, F. Paul, and M Hoelzle (2006), Strong spatial variability of snow  
914 accumulation observed with helicopter borne GPR on two adjacent Alpine glaciers,  
915 *Geophysical Research Letters*, 33(13), doi:10.1029/2006GL026576.

916 Murakami, H., Chen, X., Hahn, M. S., Liu, Y., Rockhold, M. L., Vermeul, V. R., Zachara, J. M.,  
917 and Rubin, Y. (2010), Bayesian approach for three-dimensional aquifer characterization at the  
918 Hanford 300 Area, *Hydrol. Earth Syst. Sci.*, 14, 1989-2001, doi:10.5194/hess-14-1989-2010.

919 Nobrega, S, and P Grogan (2007), Deeper snow enhances winter respiration from both plant-  
920 associated and bulk soil carbon pools in birch hummock tundra, *Ecosystems*,  
921 doi:10.1007/s10021-007-9033-z.

922 Nolan, M., C. Larsen, and M. Sturm (2015), Mapping snow depth from manned aircraft on  
923 landscape scales at centimeter resolution using structure-from-motion photogrammetry,  
924 *Cryosphere*, 9(4), 1445–1463, doi:10.5194/tc-9-1445-2015.

925 Osterkamp, T. E. (2007), Causes of warming and thawing permafrost in Alaska, *Eos Trans.*  
926 *AGU*, 88(48), 522–523, doi:10.1029/2007EO480002.

927 Pomeroy, J.W., Gray, D.M. and Landine, P.G., 1993. The Prairie Blowing Snow Model:  
928 characteristics, validation, operation. *J. Hydrol.*, 144: 165-192.

929 Pomeroy, J. W., Marsh, P. and Gray, D. M. (1997), Application of a distributed blowing snow  
930 model to the Arctic. *Hydrol. Process.*, 11: 1451–1464. doi:10.1002/(SICI)1099-  
931 1085(199709)11:11<1451::AID-HYP449>3.0.CO;2-Q

932 Proksch, M., Löwe, H. and Schneebeli, M. (2015), Density, specific surface area, and correlation  
933 length of snow measured by high-resolution penetrometry. *J. Geophys. Res. Earth Surf.*, 120:  
934 346–362. doi: 10.1002/2014JF003266.

935 Rees, A., English, M., Derksen, C., Toose, P. and Silis, A. (2014), Observations of late winter  
936 Canadian tundra snow cover properties. *Hydrol. Process.*, 28: 3962–3977.  
937 doi:10.1002/hyp.9931

938 Ribeiro, P.J., Diggle, P.J. (2001). *geoR: a package for geostatistical analysis*. 15-18. ISSN R-  
939 NEWS 1 (2), 1609–3631.

940 Smith, M.J., J. Chandler, and J. Rose (2009), High spatial resolution data acquisition for the  
941 geosciences: kite aerial photography, *Earth Surf. Proc. and Land.*, 34(1), 155-161.

942 Stieglitz, M., S.J.De ´ry, V. E. Romanovsky, and T. E. Osterkamp, The role of snow cover in the  
943 warming of arctic permafrost, *Geophys. Res. Lett.*, 30(13), 1721,  
944 doi:10.1029/2003GL017337, 2003.

945 Sturm, M., and A. M. Wagner (2010), Using repeated patterns in snow distribution modeling: An  
946 Arctic example, *Water Resour. Res.*, 46, W12549, doi:10.1029/2010WR009434.

947 Schimel, J. P., Bilbrough, C., & Welker, J. M. (2004). Increased snow depth affects microbial  
948 activity and nitrogen mineralization in two Arctic tundra communities. *Soil Biology and*  
949 *Biochemistry*, 36(2), 217-227.

950 Sjögersten, S., van der Wal, R., and Woodin, S. J. (2006). Small-scale hydrological variation  
951 determines landscape CO<sub>2</sub> fluxes in the high Arctic. *Biogeochemistry*, 80(3), 205–216.  
952 doi:10.1007/s10533-006-9018-6.

953 Sturm, M., Schimel, J., Michaelson, G., Welker, J. M., Oberbauer, S. F., Liston, Fahnestock J.  
954 and Romanovsky, V. E. (2005). Winter biological processes could help convert arctic tundra  
955 to shrubland. *Bioscience*, 55(1), 17-26.

956 Tiuri, M. E., A. H. Sihvola, E. G. Nyfors, and M. T. Hallikaiken (1984), The complex dielectric  
957 constant of snow at microwave frequencies, *Oceanic Engineering, IEEE Journal of*, 9(5),  
958 377–382, doi:10.1109/JOE.1984.1145645.

959 Wainwright, H. M., J. Chen, D. S. Sassen, and S. S. Hubbard (2014), Bayesian hierarchical  
960 approach and geophysical data sets for estimation of reactive facies over plume scales, *Water*  
961 *Resour. Res.*, 50, 4564–4584, doi:10.1002/2013WR013842.

962 Wainwright, H. M., B. Dafflon, L. J. Smith, M. S. Hahn, J. B. Curtis, Y. Wu, C. Ulrich, J.E.  
963 Peterson, M.S. Torn, and S.S. Hubbard (2015), Identifying multi scale zonation and assessing  
964 the relative importance of polygon geomorphology on carbon fluxes in an Arctic tundra  
965 ecosystem, *J. Geophys. Res. Biogeosci.*, 120, 788–808, doi:10.1002/2014JG002799.

966 Wainwright, H. M., A. Flores Orozco, M. Bückner, B. Dafflon, J. Chen, S. S. Hubbard, and K. H.  
967 Williams (2016), Hierarchical Bayesian method for mapping biogeochemical hot spots using  
968 induced polarization imaging, *Water Resour. Res.*, 52, doi:10.1002/2015WR017763.

969 Wikle, C. K., R. F. Milliff, D. Nychka, and L. M. Berliner (2001), Spatiotemporal hierarchical  
970 Bayesian modeling: Tropical ocean surface winds, *J. Am. Stat. Assoc.*, 96(454), 382–397.

971 Zhang, T. J. (2005). Influence of the seasonal snow cover on the ground thermal regime: An  
972 overview. *Reviews of Geophysics* 43: RG4002. doi:10.1029/2004RG000157.

973 Zona, D., D. A. Lipson, R. C. Zulueta, S. F. Oberbauer, and W. C. Oechel (2011),  
974 Microtopographic controls on ecosystem functioning in the Arctic Coastal Plain, *J. Geophys.*  
975 *Res. Biogeo.* (2005–2012), 116(G4).

976 Zona, D., Gioli, B., Commane, R., Lindaas, J., Wofsy, S. C., Miller, C. E., ... & Chang, R. Y. W.  
977 (2016). Cold season emissions dominate the Arctic tundra methane budget. *Proceedings of the*  
978 *National Academy of Sciences*, 113(1), 40-45.

979 **List of Figures**

980 Figure 1. (a) Location of Barrow, Alaska, USA, and Barrow Environmental Observatory (BEO)  
981 from Hubbard et al. (2013). (b) NGEE-Arctic site with the digital elevation map from the  
982 airborne LiDAR (in meters). The black boxes are the intensive sampling plots (Plot A, B, C and  
983 D). The white rectangles are the fine-grid snow depth measurements by a snow depth probe. The  
984 three black lines represent the 500-meter transects.

985

986 Figure 2. Radar velocity as a function of (a) co-located snow depth measured by a snow depth  
987 probe and (b) elevation difference (i.e., topographic variability) within 1 m. (c) Comparison  
988 between the probe-derived and GPR-derived snow depth at all the co-located locations (blue  
989 circles) and at selected locations (red circles) where topographic variability is low. In (a), the  
990 black vertical line is the median snow depth, and the dotted lines are  $\pm$  one STDEV from the  
991 median snow depth. In (b), the black line is the cut-off elevation difference of 0.05 m.

992

993 Figure 3. Elevation and snow depth in Plots A, B, C and D. The left column is LiDAR DEM (in  
994 meters), the middle column is the probe measured snow depth (in meters), and the right column  
995 is the interpolated snow depth estimated using GPR (in meters).

996

997 Figure 4. (a) PhoDAR-derived DSM in meters (August, 2014), b) PhoDAR-derived snow depth  
998 in meters (May, 2015), and (c) comparison between the PhoDAR-based and probe-based snow  
999 depth at all the locations (blue circles) and at selected locations (red circles) having low  
1000 topographic variability (the sub-meter elevation variability less than 0.05 m). The black line in  
1001 (b) represents the snow depth probe measurements every 3 meter along the 500-meter transect.

1002 Figure 5. Boxplots of (a) snow depth and (b) elevation and (c) microtopographic elevation in  
1003 Plots A-D.

1004

1005 Figure 6. Correlation coefficients between snow depth and topographic metrics as a function of  
1006 the wavelet scale: (a) the microtopographic elevation, and (b) the wind factor of  
1007 macrotopography. The different colors represent different plots (Plot A–D) or all the data (All).  
1008 Each dash line represents the scale that maximize the magnitude of the correlation coefficient.

1009

1010 Figure 7. The estimated mean snow depth across the site (in meters) based on (a) the proposed  
1011 Bayesian method including the correlation to microtopography, and (b) the kriging-based  
1012 interpolation of the snow surface. The spatial extent is the same as Figure 1b.

1013

1014 Figure 8. The estimated standard deviation of snow depth across the site (in meters) based on (a)  
1015 the proposed Bayesian method including the correlation to microtopography, and (b) the kriging-  
1016 based interpolation of the snow surface. The spatial extent is the same as Figure 1b.

1017

1018 Figure 9. Estimated mean and confidence intervals from the Bayesian method, compared to the  
1019 probe-measured snow depth by (a) using the correlation to microtopography and (b) interpolating  
1020 the snow surface. The red circles represent the snow depth at the validation locations (the snow  
1021 depth probe measurements not used in the estimation), the blue lines are the confidence intervals  
1022 based on the standard deviation (STD) multiplied by 1.9 (94% confidence intervals), and the  
1023 black lines are the one-to-one line.

1024

1025 **List of Tables**

1026 Table 1. Multivariate normal distribution defined for each variable.

1027

1028 Table 2. Root mean squared error (RMSE) between the PhoDAR-derived DSM and GPS

1029 elevation measurements based on the three schemes: nearest neighbor, average, and minimum

1030 elevation within the 0.5 m radius.

1031

1032 Table 3.  $p$  values from Tukey's pairwise comparison test for each pair of the plots.

1033

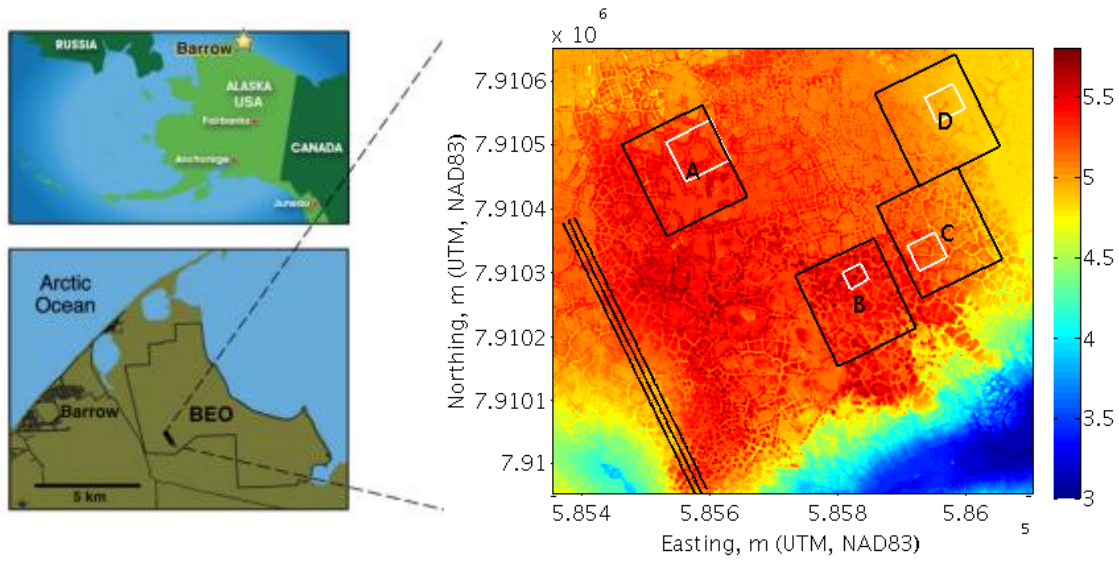
1034 Table 4. Estimated geostatistical parameters and covariance models for snow depth, snow

1035 surface and residual snow depth.

1036

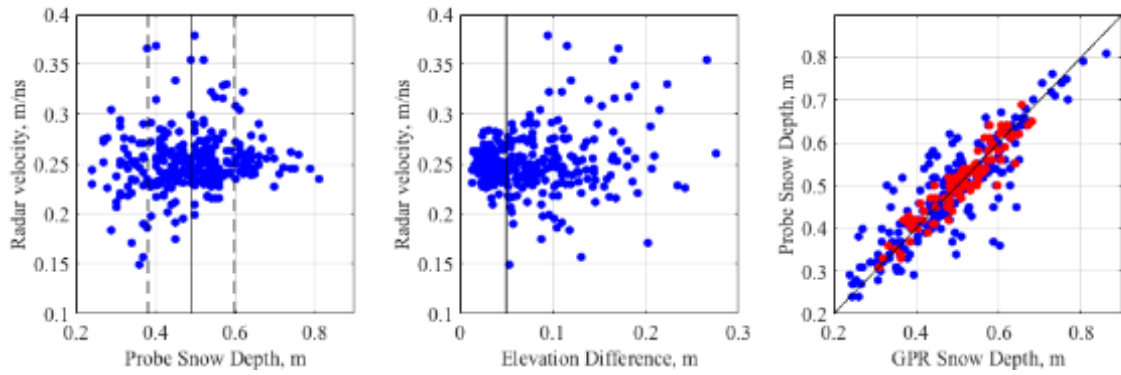
1037 Table A.1. Posterior distributions during the Gibbs sampling.

1038



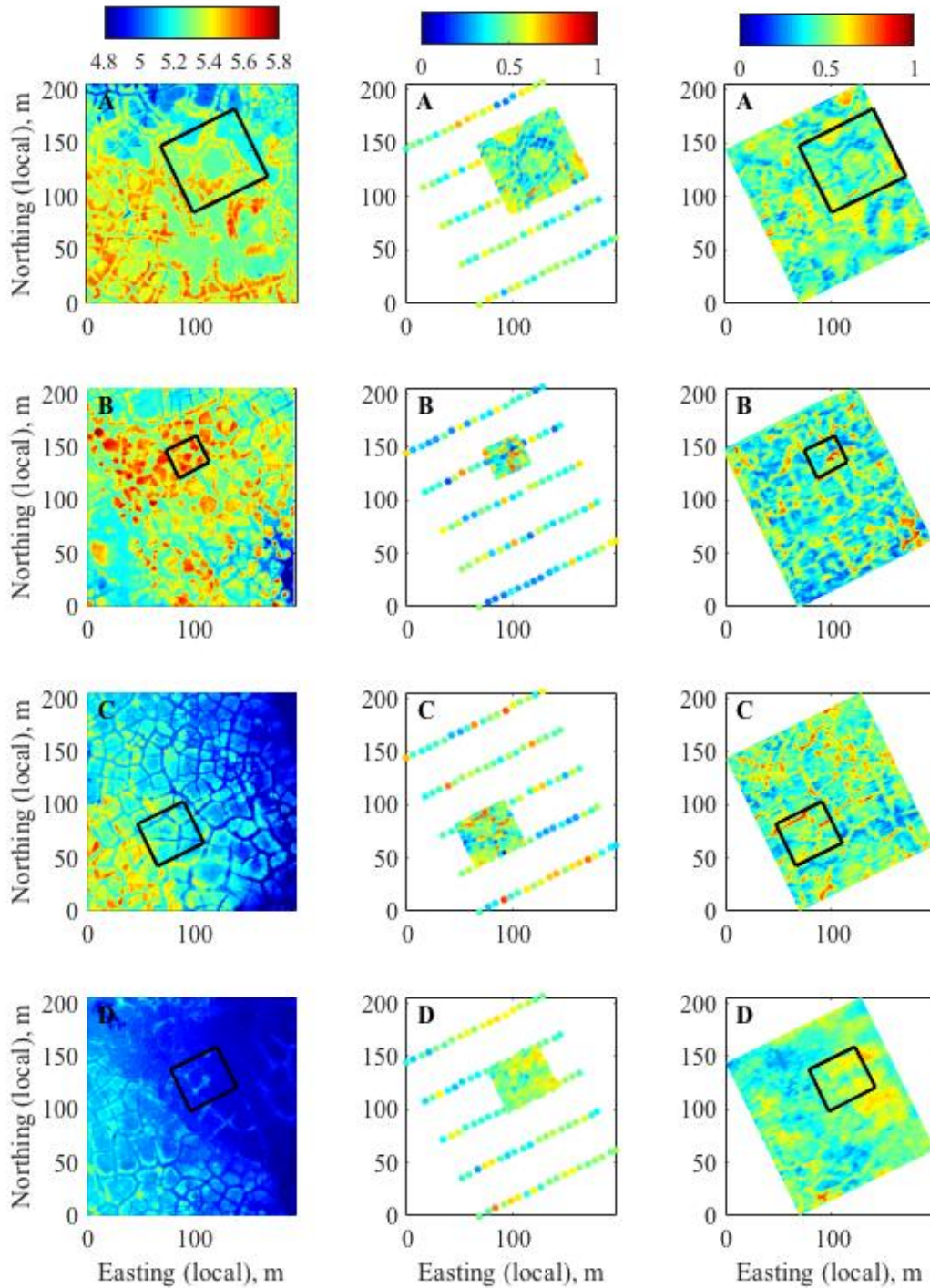
1039  
 1040  
 1041  
 1042  
 1043  
 1044  
 1045  
 1046

(a) (b)  
 Figure 1. (a) Location of Barrow, Alaska, USA, and Barrow Environmental Observatory (BEO) from Hubbard et al. (2013). (b) NGEE-Arctic site with the digital elevation map from the airborne LiDAR (in meters). The black boxes are the intensive sampling plots (Plot A, B, C and D). The white rectangles are the fine-grid snow depth measurements by a snow depth probe. The three black lines represent the 500-meter transects.

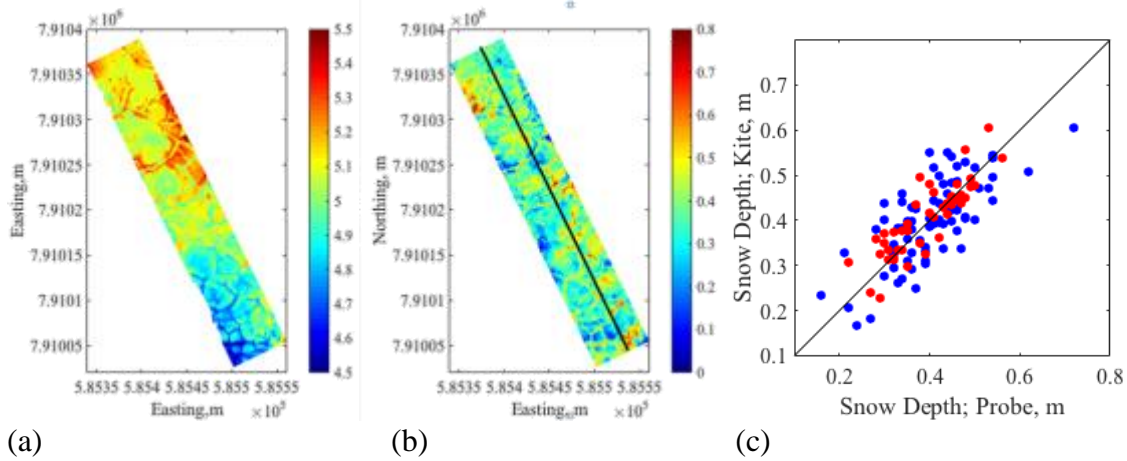


1047  
 1048  
 1049  
 1050  
 1051  
 1052  
 1053  
 1054  
 1055

(a) (b) (c)  
 Figure 2. Radar velocity as a function of (a) co-located snow depth measured by a snow depth probe and (b) elevation difference (i.e., topographic variability) within 1 m. (c) Comparison between the probe-derived and GPR-derived snow depth at all the co-located locations (blue circles) and at selected locations (red circles) where topographic variability is low. In (a), the black vertical line is the median snow depth, and the dotted lines are  $\pm$  one STDEV from the median snow depth. In (b), the black line is the cut-off elevation difference of 0.05 m.

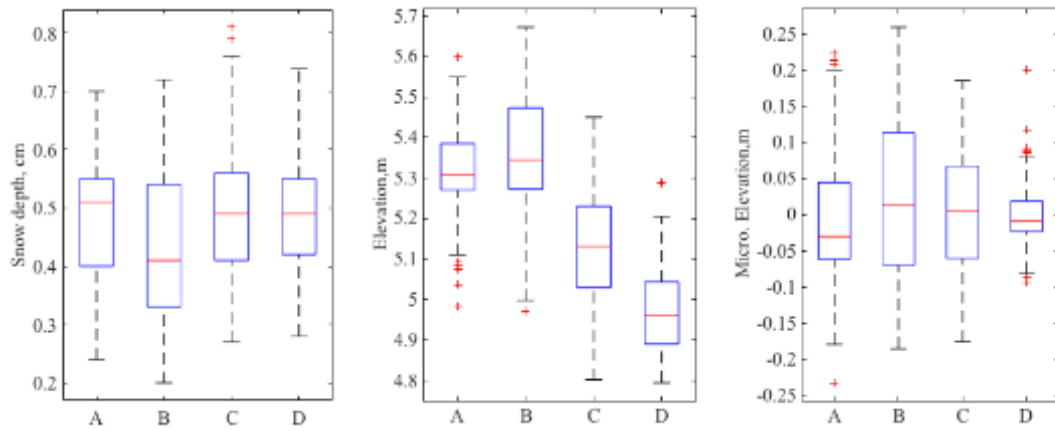


1056  
 1057 Figure 3. Elevation and snow depth in Plots A, B, C and D. The left column is LiDAR DEM (in  
 1058 meters), the middle column is the probe-measured snow depth (in meters), and the right column  
 1059 is the interpolated snow depth estimated using GPR (in meters). The black boxes represent the  
 1060 locations of the fine-grid snow depth measurements.  
 1061

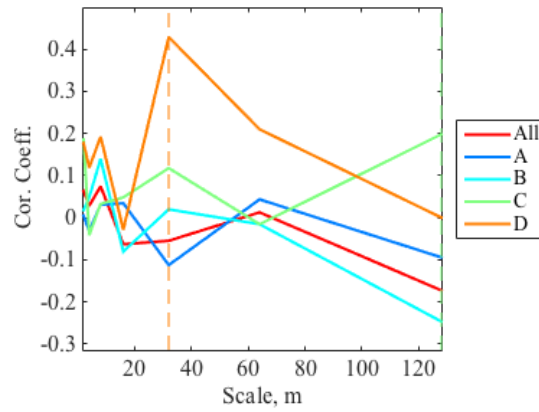
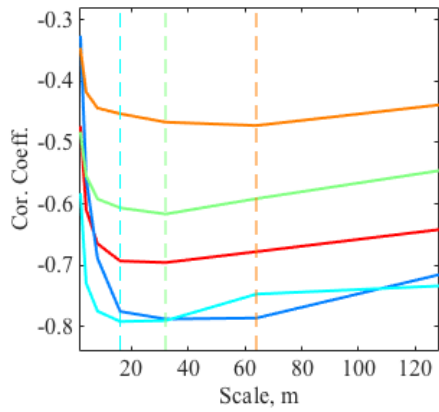


1062  
 1063  
 1064  
 1065  
 1066  
 1067  
 1068  
 1069  
 1070

(a) PhoDAR-derived DSM in meters (August, 2014), (b) PhoDAR-derived snow depth in meters (May, 2015), and (c) comparison between the PhoDAR-based and probe-based snow depth at all the locations (blue circles) and at selected locations (red circles) having low topographic variability (the sub-meter elevation variability less than 0.05 m). The black line in (b) represents the 183 snow depth probe measurements every 3 meter along the 500-meter transect.

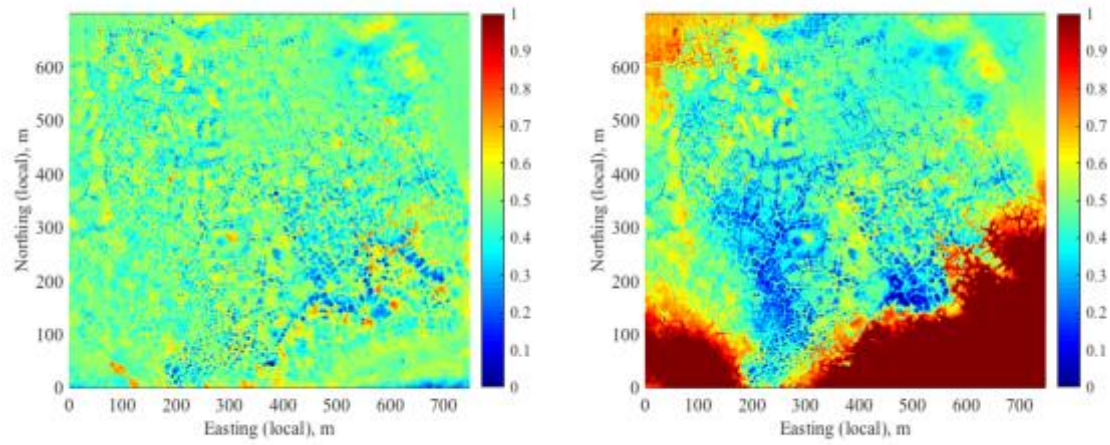


1071 (a) (b) (c)  
 1072 Figure 5. Boxplots of (a) snow depth and (b) elevation and (c) microtopographic elevation in  
 1073 Plots A-D.  
 1074  
 1075



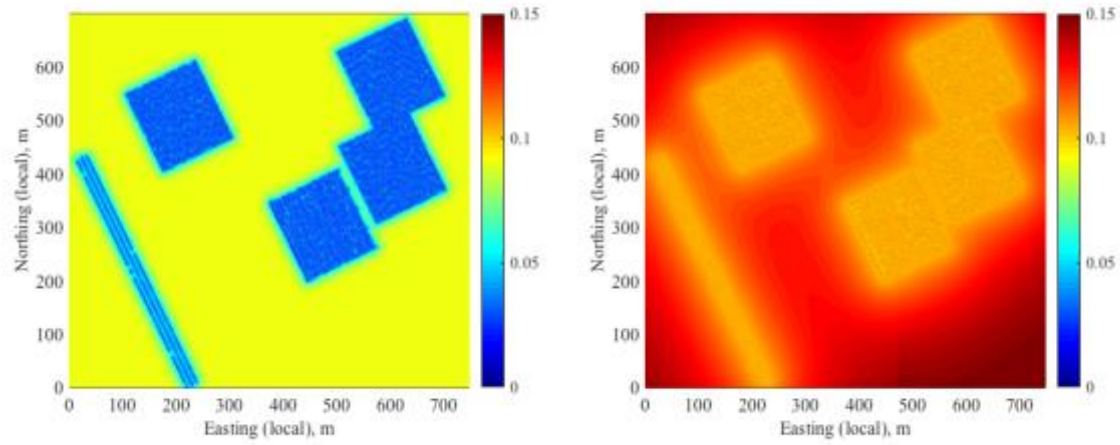
1076  
1077  
1078  
1079  
1080  
1081

(a) (b)  
Figure 6. Correlation coefficients between snow depth and topographic metrics as a function of the wavelet scale: (a) the microtopographic elevation, and (b) the wind factor of macrotopography. The different colors represent different plots (Plots A–D) or all the data (All). Each dash line represents the scale that maximize the magnitude of the correlation coefficient.

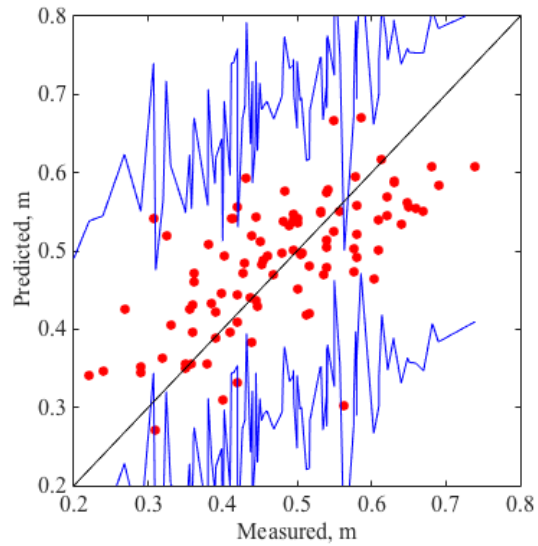
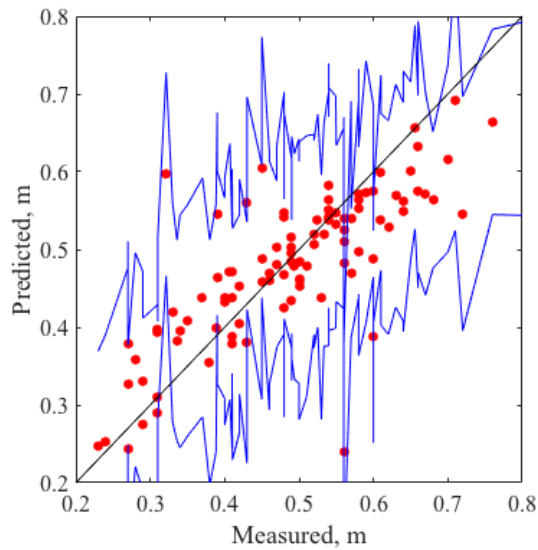


1082  
 1083  
 1084  
 1085  
 1086  
 1087

(a) (b)  
 Figure 7. The estimated mean snow depth over the NGEE-Arctic site (in meters) based on (a) the proposed Bayesian method including the correlation to microtopography, and (b) the kriging-based interpolation of the snow surface. The spatial extent is the same as Figure 1b.



1088  
 1089 (a) (b)  
 1090 Figure 8. The estimated standard deviation of snow depth across the site (in meters) based on (a)  
 1091 the proposed Bayesian method including the correlation to microtopography, and (b) the kriging-  
 1092 based interpolation of the snow surface. The spatial extent is the same as Figure 1b.  
 1093



1094  
 1095  
 1096  
 1097  
 1098  
 1099  
 1100  
 1101  
 1102  
 1103  
 1104

(a) (b)  
 Figure 9. Estimated mean and confidence intervals from the Bayesian method, compared to the probe-measured snow depth by (a) using the correlation to microtopography and (b) interpolating the snow surface. The red circles represent the snow depth at the validation locations (the snow depth probe measurements not used in the estimation), the blue lines are the confidence intervals based on the standard deviation (STD) multiplied by 1.9 (94% confidence intervals), and the black lines are the one-to-one line.

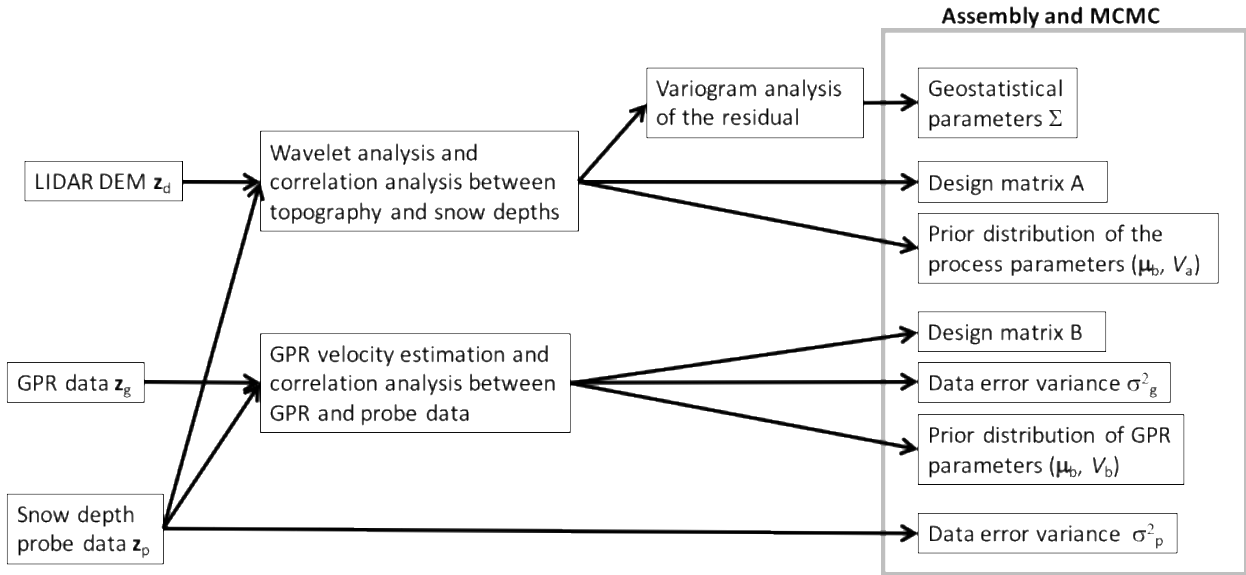


Figure B.1. Workflow of the Bayesian geostatistical estimation.

1105  
1106  
1107  
1108

1109 Table 1. Multivariate normal distribution defined for each variable.

Variable		Type	Distribution	Covariance	Mean vector
Snow depth	$\mathbf{y}$	Process model	$p(\mathbf{y} \mathbf{a}, z_d)$	$\Sigma$	$\mathbf{A}\mathbf{a}$
Probe data	$z_p$	Data model	$p(z_p \mathbf{y})$	$\mathbf{D}_p$	$\mathbf{y}$
GPR data	$z_g$	Data model	$p(z_g \mathbf{y}, \mathbf{b})$	$\mathbf{D}_g$	$\mathbf{B}\mathbf{y} + b_0$
Snow-depth parameters	$\mathbf{a}$	Prior	$p(\mathbf{a})$	$\mathbf{V}_a$	$\boldsymbol{\mu}_a$
GPR parameters	$\mathbf{b}$	Prior	$p(\mathbf{b})$	$\mathbf{V}_b$	$\boldsymbol{\mu}_b$

1110

1111 Table 2. Root mean squared error (RMSE) between the PhoDAR-derived DSM and RTK DGPS  
1112 elevation measurements based on the three schemes: nearest neighbor, average, and minimum  
1113 elevation within the 0.5 m radius.

	Nearest (cm)	Average (cm)	Minimum (cm)
July 2013	6.88	6.41	6.62
August 2014	6.40	6.19	6.34

1114

1115 Table 3. *p* values from Tukey's pairwise comparison test for each pair of the plots.

	Snow depth
Plot A – Plot B	<b><math>6.34 \times 10^{-3}</math></b>
Plot A – Plot C	0.982
Plot A – Plot D	0.998
Plot B – Plot C	<b><math>1.72 \times 10^{-3}</math></b>
Plot B – Plot D	<b><math>3.55 \times 10^{-3}</math></b>
Plot C – Plot D	0.997

1116

1117

1118 Table 4. Estimated geostatistical parameters and covariance models for snow depth, snow  
1119 surface and residual snow depth.

	Model	Range (m)	Variance (m <sup>2</sup> )	Nugget Ratio
Snow depth	Exponential	12.3	$1.6 \times 10^{-2}$	0.0
Snow surface	Spherical	253.3	$2.0 \times 10^{-2}$	0.16
Residual snow depth	Exponential	15.0	$8.3 \times 10^{-3}$	0.0

1120

1121 Table A.1. Posterior distributions during the Gibbs sampling

Variable		Covariance, Q	Mean vector
Snow depth	$\mathbf{y}$	$(\mathbf{B}^T \mathbf{D}_g^{-1} \mathbf{B} + \mathbf{D}_p^{-1} + \Sigma^{-1})^{-1}$	$\mathbf{Q}(\mathbf{B}^T \mathbf{D}_g^{-1} (\mathbf{z}_g - \mathbf{b}_0) + \mathbf{D}_p^{-1} \mathbf{z}_p + \Sigma^{-1} \mathbf{A} \mathbf{a})$
Snow depth parameters	$\mathbf{a}$	$(\mathbf{A}^T \Sigma^{-1} \mathbf{A} + \mathbf{V}_a^{-1})^{-1}$	$\mathbf{Q}(\mathbf{A}^T \Sigma^{-1} \mathbf{y} + \mathbf{V}_a^{-1} \boldsymbol{\mu}_a)$
GPR parameters	$\mathbf{b}$	$(\mathbf{H}^T \mathbf{D}_g^{-1} \mathbf{H} + \mathbf{V}_b^{-1})^{-1}$	$\mathbf{Q}(\mathbf{B}^T \mathbf{D}_g^{-1} (\mathbf{z}_g - \mathbf{b}_0) + \mathbf{V}_b^{-1} \boldsymbol{\mu}_b)$

1122  
1123